International Journal of Precision Engineering and Manufacturing-Green Technology (2023) 10:381–408
https://doi.org/10.1007/s40684-022-00462-8

Online ISSN 2198-0810
Print ISSN 2288-6206

REGULAR PAPER

Comprehensive Study on the Cutting Force Modeling and Machinability of High Frequency Electrical Discharge Assisted Milling Process Using a Novel Tool

Moran Xu[1,2] · Rong Wei[2] · Changping Li[2] · Rendi Kurniawan[1] · Jielin Chen[1] · Tae Jo Ko[1]

Received: 6 June 2022 / Revised: 31 July 2022 / Accepted: 13 August 2022 / Published online: 15 September 2022

Abstract

Previous research had validated the machinability of the new machining method of electrical discharge assisted milling (EDAM). However, the EDAM tool has shortcomings, such as its inability to compensate for the electrodes and small discharge area, which restricted further popularization and applications of the method. So, this research introduced a high frequency EDAM (HF-EDAM), based on a novel tool with flexible electrodes. Notably, the material removal mechanism of HF-EDAM under different machining parameters was deeply explored in this study. In particular, the discharge signal, electrode and workpiece surface topographies, cutting force, tool wear, and machined-surface integrity of HF-EDAM were analyzed to find the machining mechanism of HF-EDAM under different machining parameters. At the same time, a two-dimensional cutting force model of HF-EDAM was also established, and a series of experiments showed that the model had good prediction accuracy for cutting forces. Furthermore, the experiments also showed that the HF-EDAM greatly reduced the cutting force and tool wear, and improved the machined-surface integrity as compared to those under CM, respectively. In essence, the excellent machinability of HF-EDAM was verified by experiments and modeling. Hence, HF-EDAM is an effective method for high-quality and efficient machining of titanium alloys, which are difficult to machine.

Keywords Titanium alloy · Flexible electrode · Electrical discharge assisted milling · Surface integrity · Hybrid machining

1 Introduction

Titanium alloys are attractive materials because of their corrosion resistance, high specific strength, low density, and good mechanical properties, and widely used in high-end fields, such as aerospace, chemical energy, and medical devices [1, 2]. However, a titanium alloy has a low heat transfer coefficient, high chemical activity, and large frictional coefficient, which easily produce temperature gradients within the alloy during its conventional machining. Consequently, the temperature gradients result in low machining-efficiency and poor machined-surface-integrity. In addition, titanium alloys are typically difficult-to-machine materials [3]. In this context, various hybrid machining methods have emerged to improve the machinability of titanium alloys during the machining.

Generally, hybrid machining can improve the machining efficiency, tool life, and machined-surface integrity as compared to those under any conventional machining, respectively [4, 5]. Relatedly, Niu et al. [6] investigated a longitudinal torsional ultrasonic vibration milling of titanium alloys (Ti6Al4V) and conducted orthogonal experiments to evaluate the effect of machining parameters on the machined material. Studies have also shown that ultrasonic-vibration assisted milling is an effective way to machine titanium alloys. In particular, the machining efficiency and machined-surface quality of the milling have improved with ultrasonic vibration assistance to a certain extent as compared to those under CM, respectively, especially to result in machined-surface compressive stresses.

✉ Changping Li
15073200235@163.com

✉ Tae Jo Ko
tjko@yu.ac.kr

[1] School of Mechanical Engineering, Yeungnam University, 280 Daehak-ro, Gyoungsan-si, Gyeongsangbuk-do 38541, Republic of Korea

[2] College of Mechanical and Electrical Engineering, Hunan University of Science and Technology, Xiangtan 411201, China

Yadav and Yadava [7] proposed an electrical discharge drilling (EDD) to machine aerospace titanium alloys and used new hybrid modeling to determine the material surface removal rate (MRR), average machined-surface roughness (Ra), average drilled-hole-roundness (Ca), and other parameters of the EDD for the machining optimization. In particular, the MRR, Ra, and Ca of the EDD had increased by 30.80%, 24.81%, and 26.09% as compared to those under conventional EDM, respectively. Likewise, Ayed et al. [8] investigated laser-assisted machining (LAM) of Ti6Al4V and compared the experiments and simulations on the machining. This investigation showed that the LAM could effectively reduce the cutting force and significantly improve the productivity by optimizing the cutting conditions, compared to those under any conventional machining, respectively. However, ultrasonic-vibration assisted machining has disadvantages, such as simultaneous high machined-surface-roughness and poor machining-accuracy.

Meanwhile, EDM hybrid machining has significantly improved the machining efficiency and accuracy of difficult-to-machine materials, compared to those under conventional machining [9–11]. For example, EDM hybrid machining is widely used to machine titanium alloys because of its high machining-efficiency, indirect contact between the electrode and the workpiece, and longer tool life, and has more advantages as compared to laser-assisted machining [12]. Relatedly, Kurniawan et al. [13] proposed an ultrasonic-assisted dry discharge machining (USEDAM) in a gaseous medium. Their machining showed that the ultrasonic vibration by USEDAM resulted in a higher burr-removal rate (BRR) of the machining than that of dry EDM. Likewise, Li et al. [14] proposed hybrid machining (EDM and end milling) as effective machining for difficult-to-machine materials. In particular, the machined-surface quality had improved in the hybrid, EDM and end milling as compared to that in CM.

Li et al. [15, 16] proposed an electrical discharge assisted milling (EDAM). Further, Xu et al. [17] systematically studied the machined-surface integrity in EDAM of titanium alloys, under multi-parameters, including the machined-surface morphology, roughness, residual stress, and microhardness. Their study showed that the machined-surface integrity in the EDAM had improved effectively compared to that under CM. However, EDAM tools based on ordinary electrodes have some disadvantages, such as their inability to match the electrode surfaces in real-time according to the changes in the machining parameters and compensate the electrodes in real-time according to the electrode consumption. Additionally, the small electrode-area and low discharge ratio of the EDAM tool also inhibit the promotion of EDAM.

A new, HF-EDAM, based on a novel tool with flexible electrodes, is presented in this article. Notably, the unique properties, flexibility and mesh structure, of the flexible electrodes had been used in designing a special, new EDAM tool for HF-EDAM. Furthermore, the machining mechanism of the flexible electrodes in HF-EDAM is discussed in depth in this article. Subsequently, a comparison of HF-EDAM with CM and HF-EDAM with non-flexible electrodes was made in terms of the discharge signal, electrode and workpiece surface topographies, cutting force, tool wear, and machined-surface integrity, under different machining parameters.

Meanwhile, the machining characteristics of the complex discharge process and the short reaction time in HF-EDAM make it difficult to understand the machining mechanism of HF-EDAM through experiments. Therefore, a cutting force model of HF-EDAM was also developed. The subsequent model predictions showed that simultaneously the discharge process was more stable, the discharge time was longer, the cutting force was effectively reduced, and the machined-surface integrity was improved in HF-EDAM as compared to those under the other two machining methods, respectively. Furthermore, the experimental results of this study on the HF-EDAM and the other two machining methods were consistent with the corresponding model predictions. Hence, this study provides new hybrid machining (HF-EDAM) for titanium alloys, and has improved the promotion and application of HF-EDAM.

2 Experimental Details

2.1 The Principle of HF-EDAM

Figure 1 shows the discharge process and structure of a flexible electrode EDM. In particular, Fig. 1a shows a schematic EDM using the flexible electrode. Relatedly, the flexible electrode and the workpiece are connected to the negative and positive poles of the power supply, respectively. Also, the flexible electrode and workpiece are separated by a dielectric to form a discharge gap and apply a voltage between them. As the voltage between the flexible electrode and workpiece increases, the electric field strength between them increases, causing the dielectric to break down and arcing between the flexible electrode and workpiece. The workpiece is then melted by the high temperature of the discharge to form small fragments of the workpiece, which are removed subsequently. Finally, the machined-material surface has a heat-affected layer and a recast layer.

HF-EDAM tool is a new, specially manufactured tool with a flexible electrode, for the first time. Notably, the flexible electrode improved the discharge frequency and machining performance in HF-EDAM significantly compared to those in any conventional machining or the HF-EDAM with non-flexible electrodes, respectively. Also, Fig. 1b, c show that the flexibility of the copper foam flexible electrode helps

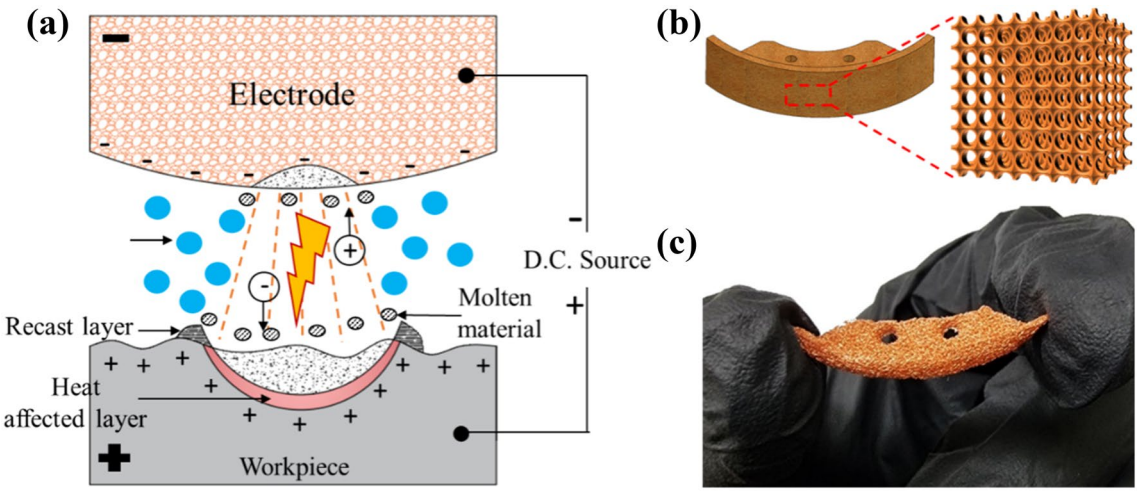

Fig. 1 Flexible electrode EDM discharge process and structure: **a** Schematic, flexible electrode EDM discharge process, **b** the copper foam flexible electrode structure, and **c** a photo of the copper foam flexible electrode

create a perfect discharge condition by adjusting the shape of the electrode surface. In addition, the unique mesh structure of the copper foam flexible electrode allows the dielectric to be integrated into the electrode during the machining process, improving the EDM efficiency greatly.

The new tool for HF-EDAM was fabricated, and the specific parameters and part details of the tool are given in Fig. 2. In particular, electric conduction between the insert holder and tool body was prevented using a plastic insulator separating them, increasing the service life of the insert significantly. In addition, the axial depth of the flexible electrodes can be adjusted using elastic gaskets.

Meanwhile, the flexible electrode of this study was fabricated with the copper foam made by Suzhou Jashide Metal Foam Co., and the insert was tungsten carbide fabricated by Taegu Tec Ltd. (SPMX050204SM). During the experiments, the porosity and pore size of copper foam were chosen to be moderate (copper foam with a porosity of 95.7% and aperture is 100 ppi) in order to maintain the flexibility and porosity of the electrode, while taking into account the stiffness and service life of the electrode. Mathematically, the electrode surface geometry can be expressed as:

$$S_{electrode} = \begin{cases} rsin(\omega t) + x_{feet}t \\ rcos(\omega t) + y_{feet}t \end{cases} \quad (1)$$

where r, t, and ω are the cutting radius, time, and angular speed of the tool rotation, respectively.

Also, the electrodes do not touch the workpiece during the EDM in HF-EDAM because a discharge gap between the electrodes and workpiece is required to generate sparks for the EDM. Therefore, the outer diameter of the electrode (D_1) is kept smaller than that of the milling insert (D_2) to generating the discharge gap. So, the relationship between the discharge gap (L_{gap}), D_1, and D_2 is:

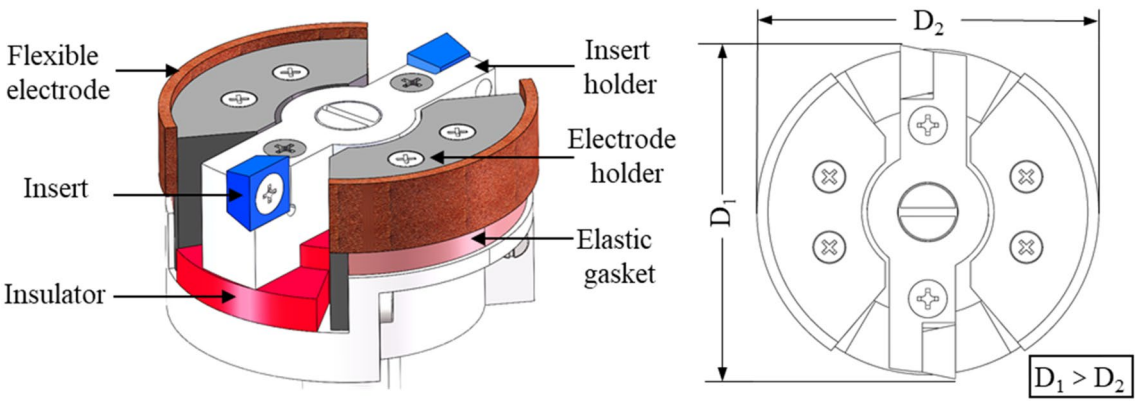

Fig. 2 The HF-EDAM tool

$$L_{gap} = \frac{1}{2}(D_1 - D_2). \quad (2)$$

Generally, the discharge gap in the EDM is determined by various factors, including the discharge energy, electrode and workpiece materials, and the type of dielectric of the EDM. In addition, the discharge time can be adjusted by adjusting the flexible electrode surface area. Meanwhile, the new HF-EDAM tool was designed to avoid the interaction between milling and EDM during machining. Likewise, the discharge time and energy can be adjusted conveniently and accurately with this tool. Additionally, this design eliminates the galvanic loss of the cutting edge caused by the discharge energy.

Figure 3 shows a schematic HF-EDAM process. In particular, Fig. 3a shows the EDM in the HF-EDAM process. Relatedly, the flexible electrode forms a stable discharge gap with the workpiece surface, and the workpiece is softened by the EDM and converted into a free-cutting layer (recast and heat-affected layers). Also, Fig. 3b shows the milling in the HF-EDAM process. In particular, the free-cutting layer and a small amount of workpiece matrix are removed by the milling. Further, Fig. 3c shows that the cutting depth of each tooth is closely related to the workpiece-surface crater depth after the discharge. Also, the EDM assistance in an EDAM can effectively reduce the cutting force and extend the tool life [15].

The following equations give the relationship between the spindle speed (N), and the activation time (t_{change}) and discharge time ($t_{discharge}$), respectively.

$$t_{change} = \frac{\alpha \times 60}{2\pi \times N} \quad (3)$$

$$t_{discharge} = \frac{\beta \times 60}{2\pi \times N} \quad (4)$$

where α is the angle between the carbide insert and the discharge electrode, and β is the angle between the electrodes.

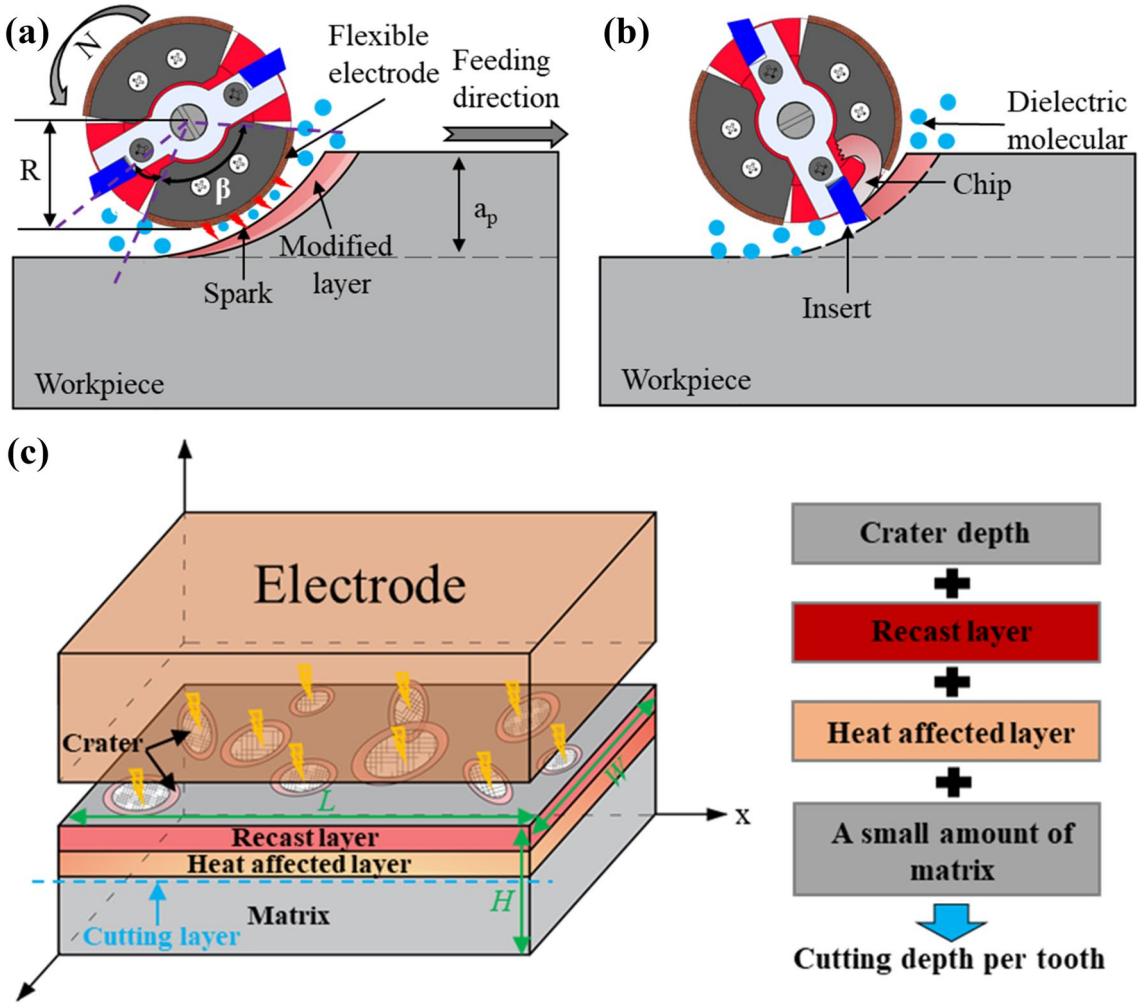

Fig. 3 Schematic HF-EDAM process: **a** the EDM in the process, **b** the milling in the process, and **c** the cutting depth definition

Therefore, the adjustment of the discharge time is inseparable from the electrode size. Further, the EDM time in the HF-EDAM process is fully improved, and the problems of tool chip removal are accounted for in the process by choosing an electrode ratio of about 75% for the HF-EDAM tool. In addition, the electrode ratio of the HF-EDAM is increased by about five times compared to that of the ordinary-electrode based EDAM tool previously designed by Li et al. [15].

Figure 4 shows the photographs of a half discharge cycle of the HF-EDAM process taken by a high-speed camera. Notably, the photographs were captured with a frame rate of 10^6 frames/s. In particular, Fig. 4 (1)–(9) shows the EDM and milling in the process, respectively. The photographs of the EDM in the process show that when a stable discharge gap is formed between the flexible electrode and the workpiece, the dielectric is broken down, and then the spark is generated continuously. Subsequently, the insert contacts the workpiece and cuts the denatured layer, as seen in the photographs of the milling in the process. So, the photographs of the EDM in the process show that the discharge of the flexible electrode is stable without any short-circuits.

The HF-EDAM tool is divided into three parts: tool body, plastic insulator, and insert holder. Plastic insulators are used to isolate the tool handle from the tool holder to prevent electric conduction between them. Meanwhile, the photographs of the milling in the HF-EDAM process show that the HF-EDAM tool protects the insert well due to the unique design insert of the tool that does not discharge during the machining. Further, the discharge time and efficiency significantly improved when the HF-EDAM tool was used for discharge in the machining as compared to those of the previous research [15].

Figure 5 compares the (previous) ordinary copper and copper foam flexible electrodes of HF-EDAM. In particular, Fig. 5 (a1), (a2), (b1), and (b2) show that when the dielectric is in contact with the ordinary copper electrode surface, the dielectric forms small water droplets on the electrode surface. On the other hand, when the dielectric is in contact

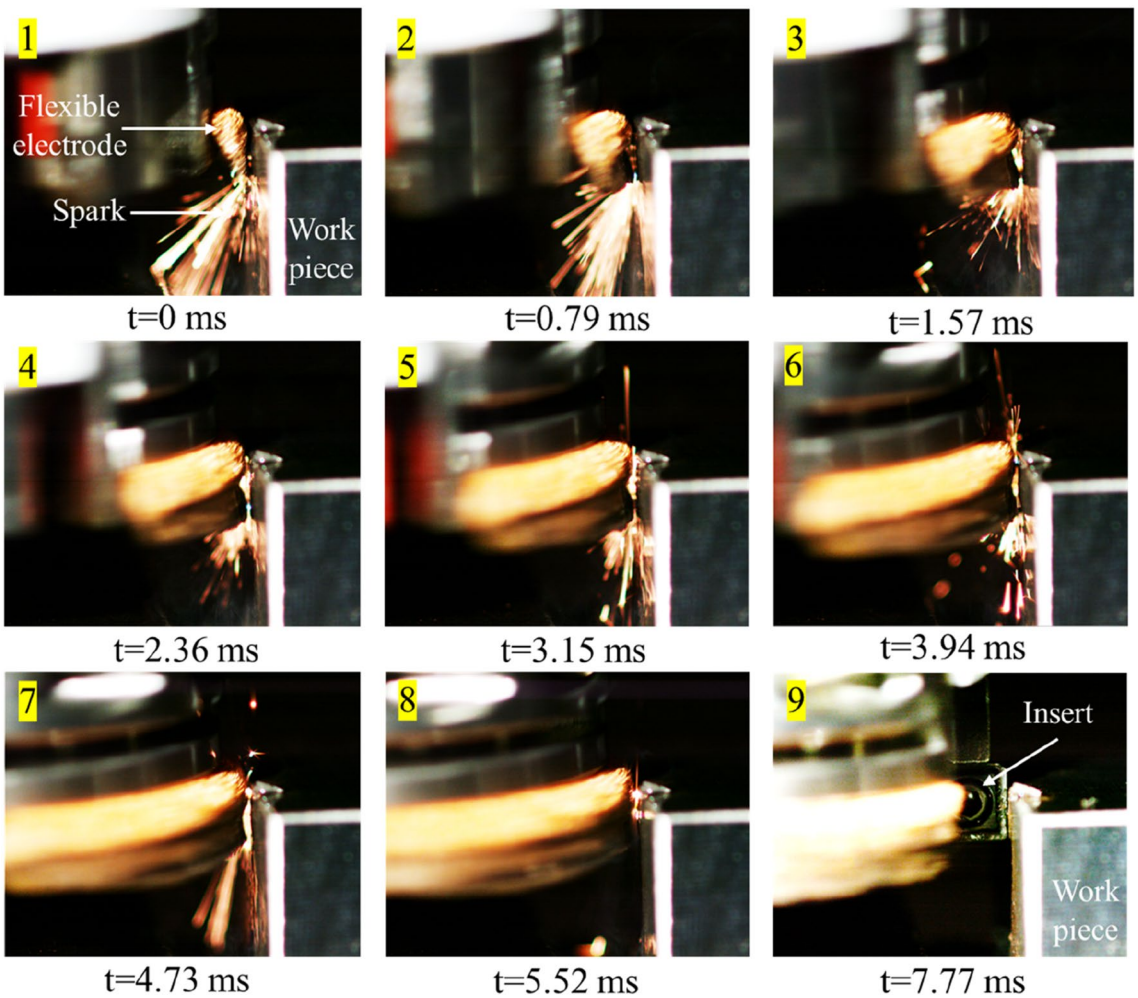

Fig. 4 Photographs of a half discharge cycle of the HF-EDAM process, taken by a high-speed camera

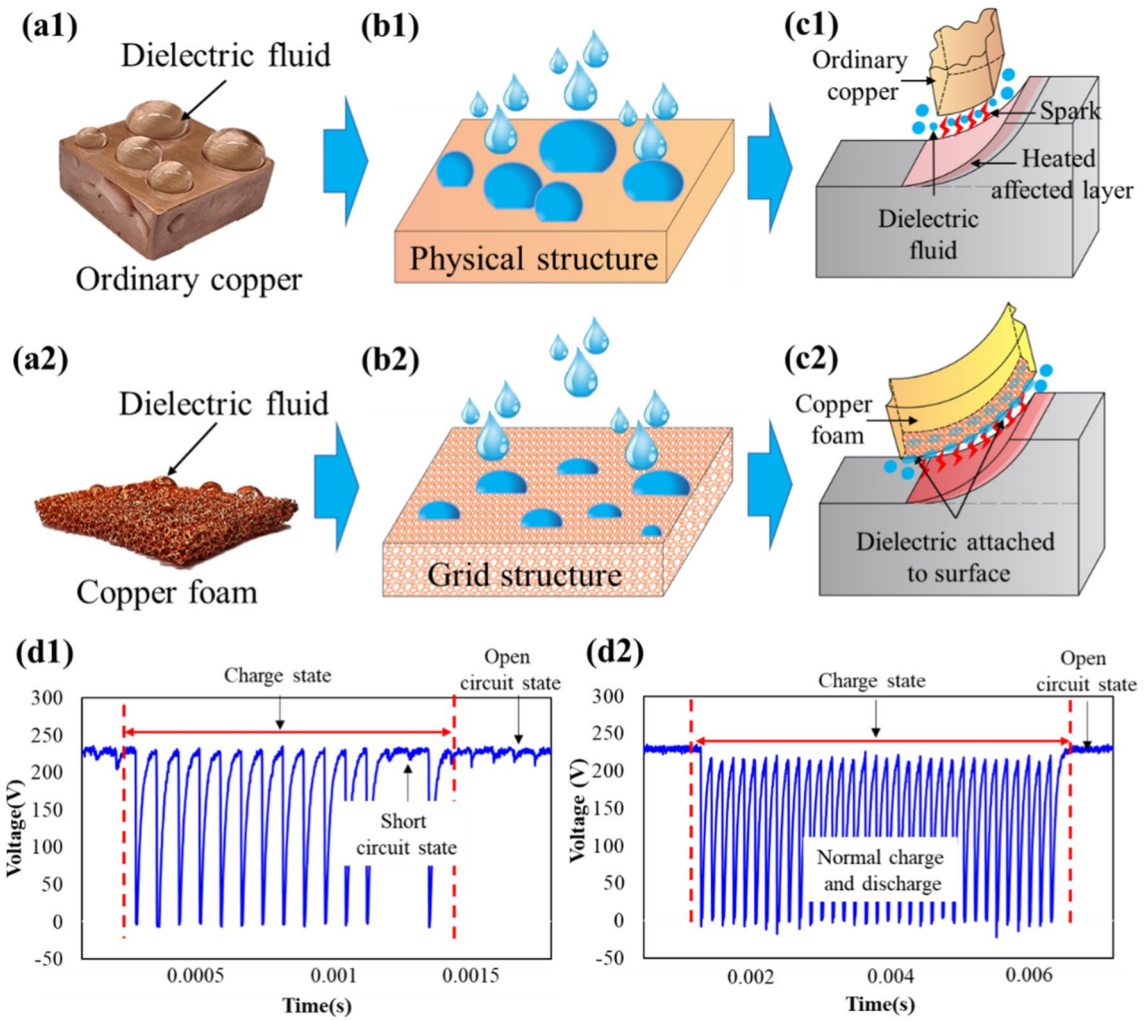

Fig. 5 Comparison of the ordinary copper and copper foam flexible electrodes of HF-EDAM.: **a1** and **a2** show the schematic of the dielectric in contact with ordinary copper and copper foam flexible cathodes; **b1** and **b2** show the microscopic diagram of the contact between the dielectric, and the ordinary copper and copper foam flexible electrodes; **c1** and **c2** show the schematic EDM with ordinary copper and copper foam flexible electrodes; and **d1** and **d2** show the discharge signal of ordinary copper and copper foam flexible electrodes, respectively

with the copper foam flexible electrode surface, the water droplets penetrate into the mesh structure of the electrode (as shown in Fig. 5 (b2)). Also, Fig. 5 (c1) and (c2) show that when the ordinary copper electrode is used in HF-EDAM to discharge, and if the electrode is in contact with the workpiece surface, a short circuit occurs. But, the dielectric penetrating into the mesh structure of the copper foam flexible electrode used in HF-EDAM for discharge makes sure the electrode contact with the workpiece surface does not affect the normal discharge (as shown in Fig. 5 (c2)).

Meanwhile, the softness of the copper foam flexible electrode allows the adjustment of the electrode surface curvature by adjusting the HF-EDAM tool, even if the electrode collides with the workpiece surface. Also, Fig. 5 (d1) and (d2) show that the discharge stability and time of the copper foam flexible electrode were better than those of the ordinary copper electrode, respectively. Finally, since a flexible electrode can be reused by adjusting the electrode surface curvature, the service life of the electrode is also much longer than that of ordinary electrodes.

Figure 6 shows the trajectory of the tool tip of the insert and the electrode, and the machined-material surface formation in HF-EDAM. In particular, Fig. 6a shows that the displacements of the abscissa and ordinate of the tool tip of the insert, $x1$ and $y1$, respectively, are:

$$x1 = v_f \times t + r1 \times \sin\left(\omega \times \mathrm{t} + \Phi_1\right), \tag{5}$$

$$\mathrm{y1} = r1 \times \cos\left(\omega \times \mathrm{t} + \Phi_1\right), \tag{6}$$

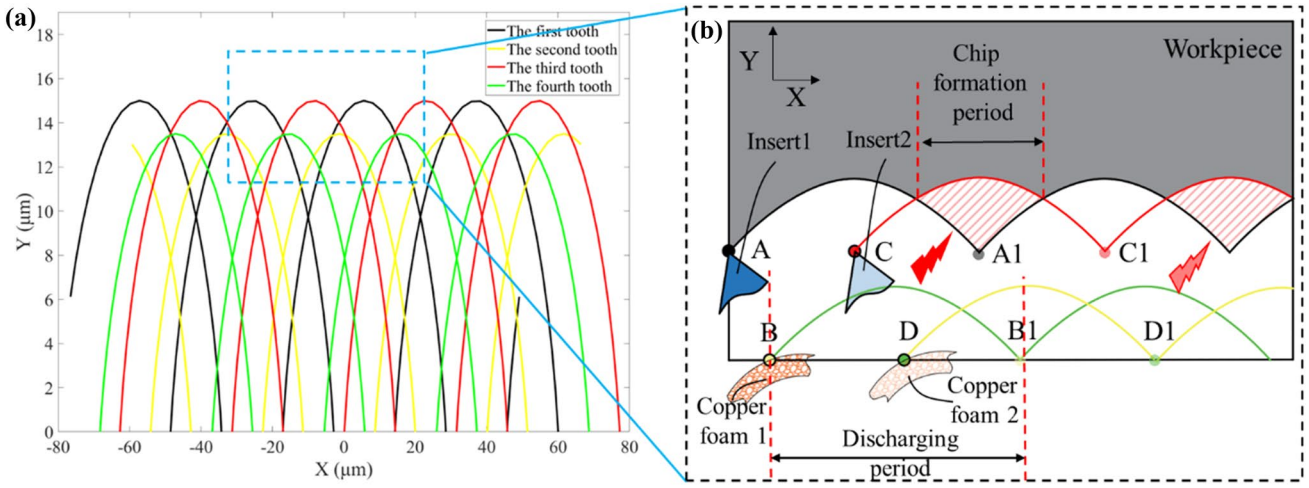

Fig. 6 **a** The trajectory of the tool tip of the insert in HF-EDAM, and **b** the machined-material surface formation in HF-EDAM

where v_f, $r1$, and Φ_1 are the feed rate, insert radius of the HF-EDAM tool, and the angle between the line connecting the tool center point and the tool tip and the Y axis, respectively.

Similarly, the displacements of the abscissa and ordinate of the flexible electrode, $x2$ and $y2$, respectively, are:

$$x2 = v_f \times t + r2 \times \sin\left(\omega \times \mathrm{t} + \Phi_2\right), \tag{7}$$

$$y2 = \mathrm{r2} \times \cos\left(\omega \times \mathrm{t} + \Phi_2\right), \tag{8}$$

where $r2$ and Φ_2 are the electrode radius of the HF-EDAM tool and the angle between the line connecting the tool center point and the electrode tip and the X axis, respectively. However, the following values were used for the different parameters to plot the trajectory given in Fig. 6 (a). The range of time was $[-2\pi, 2\pi]$, and the insert radius of the HF-EDAM tool was 15 mm. Since there is normally a discharge gap between the electrode and the workpiece (the discharge gap was 100 μm in this study), the electrode radius of the HF-EDAM tool was 14.9 mm. And the angular speed of the tool rotation was 3000 rpm. Also, the inter-tooth angles, Φ_1 and Φ_2, were 0 and 47°, respectively. Finally, the feed rate was 10 mm/min.

Figure 6 (b) shows in detail the process of machined-material surface formation in HF-EDAM. Notably, the copper foam flexible electrodes are not in contact with the machined-material surface, and there is a certain discharge gap. In essence, the feasibility of the machining mechanism of HF-EDAM is further verified by the trajectory of the tool tip of the insert in HF-EDAM.

2.2 Cutting Force Modeling of HF-EDAM

The complex discharge process of the EDM and the extremely short reaction time in HF-EDAM make it hard to find the machining mechanism of HF-EDAM under the combined action of EDM and milling by experimental methods. Therefore, this research developed, the machining mechanism of HF-EDAM by using the cutting force model of HF-EDAM. In particular, the cutting force modeling involved the following steps. First, the surface heat source of the EDM was simplified, the multi-pulse point heat-source was simplified into a uniform surface-heat-source, and the longitudinal temperature distribution curve of the workpiece material was established. Second, the cutting force coefficients affected by temperature (shear and ploughing force coefficients) were solved based on the JC constitutive model and by considering the temperatures caused by the EDM and plastic deformation of the workpiece, and the cutting force model of HF-EDAM was finally established.

2.2.1 Temperature in EDM

This research assumed that the heat generated in EDM was by the uniform heat flux in the plasma channel, as shown in Fig. 7. Notably, Fig. 7 shows that the uniform heat flux produces a microcrater on the machined-material surface.

Temperature can affect the strength of materials, especially during EDM. Relatedly, the relationship between Vickers hardness of a material and temperature is a linear function (see Fig. 8). Therefore, Vickers hardness, $H_{vickers}$, can be described in terms of temperature, T, by the following equation [18]:

$$H_{vickers} = -0.3855(T) + 350.56[HV]. \tag{9}$$

Meanwhile, the uniform heat flux in the plasma channel can be used to find the analytical solution for the microcrater temperature distribution given by the following equation [20].

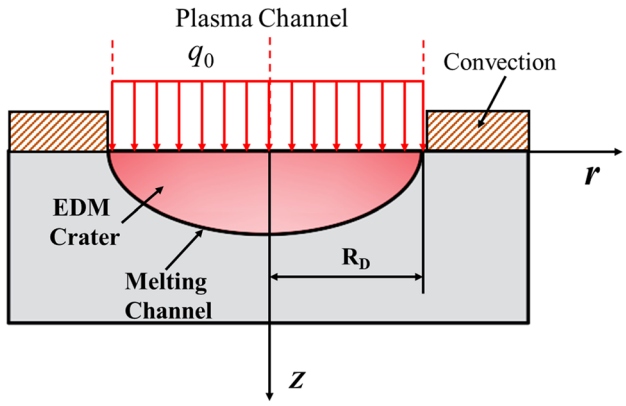

Fig. 7 Illustration of the heat generation in EDM by the uniform heat flux in the plasma channel

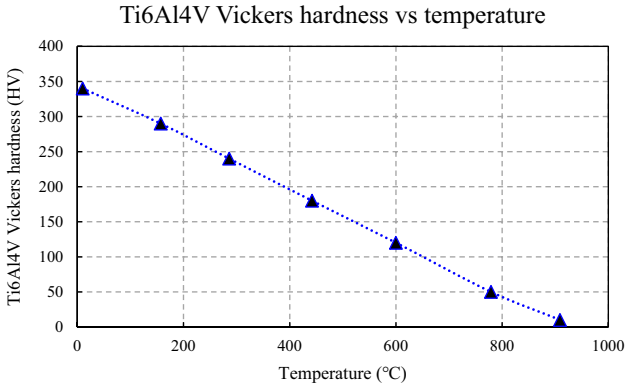

Fig. 8 Ti6Al4V Vickers hardness depending on temperature. The hardness value is a close approximation from the literature [19]

$$T(z) = \frac{2q_o\sqrt{\alpha_D \cdot t_{dis}}}{\lambda_k}\left|ierf\left(\frac{z}{2\sqrt{\alpha_D \cdot t_{dis}}}\right) - ierf\left(\frac{\sqrt{z^2 + {R_D}^2}}{2\sqrt{\alpha_D \cdot t_{dis}}}\right)\right|, \tag{10}$$

where z is the microcrater depth,q_o is the uniform heat flux density rate, α_D is the thermal diffusivity of the workpiece material, t_{dis} is the discharge time of a single plasma spark, λ_k is the thermal conductivity of the workpiece material, $ierf(z)$ is the integral complementary error function, which can be represented by the McLaughlin series:

$$ierf(z) = \sqrt{\pi}\left(\frac{1}{2}z + \frac{1}{24}\pi z^3 + \frac{7}{960}\pi^2 z^5 + \ldots\right), \tag{11}$$

and R_D is the maximum radius of the microcrater (as shown in Fig. 7). Further, the thermal diffusivity of the workpiece material can be defined as:

$$\alpha_D = \frac{\lambda_k}{\rho \cdot C_p}, \tag{12}$$

where C_p and ρ are the specific heat capacity and density of the workpiece material, respectively. Table 1 lists the thermal properties of Ti6Al4V.

Also, the RC and transistor combined circuit in the EDM in HF-EDAM has the discharge energy (E_D) expressed in the following form [20]:

$$E_D = \frac{1}{2}C_D {V_D}^2, \tag{13}$$

where C_D and V_D are the discharge capacitance and gap voltage, respectively. In addition, the discharge time of a single plasma spark can be used to express the corresponding heat flow rate, Q_D, as:

$$Q_D = \frac{E_D}{t_{dis}}. \tag{14}$$

Typically, the anode or workpiece does not absorb all the heat during the discharge. Heat is also transferred to the cathode or flexible electrode and air medium. Therefore, the rate of heat absorption by the anode, Q_a, can be expressed as:

$$Q_a = \xi \cdot Q_D, \tag{15}$$

where ξ is the percentage of heat absorbed by the anode. Jithin et al. [21] proposed different ξ values according to different discharge energy conditions. However, the $0 < E_D < 50mJ$ lead to the assuming of ξ to be 10.9% or 0.109 in this research. Further, the complex process of EDM can be simplified by considering the heat input as a uniform disk-heat-source, and the spatial distribution of heat flux density rate of the source is given by,

$$q_o = \frac{Q_a}{\pi {R_D}^2}. \tag{16}$$

Finally, the maximum radius of the microcrater predicted by previous research [22] is given by:

$$R_D(t_{dis}) = 0.788 \cdot t_{dis}^{3/4}\ [\mu m], \tag{17}$$

where 0.788 μm is the radius of the plasma channel heat source [22].

Table 2 shows that the temperature of the microcrater can be predicted by the input parameters given in the

Table 1 Thermal properties of Ti6Al4V [23]

Thermal conductivity [λ_k] W/m/°C	6.7
Specific heat capacity [C_p] J/kg/°C	542
Density [ρ] kg/m^3	4430

Table 2 Input parameters for the prediction of the microcrater temperature distribution [23]

Discharge voltage, V_D	180–80 V (chosen as 100 V)
Discharge capacitance, C_D	10,000 pF
Discharge time, t_{dis}	40, 60, and 80 µs

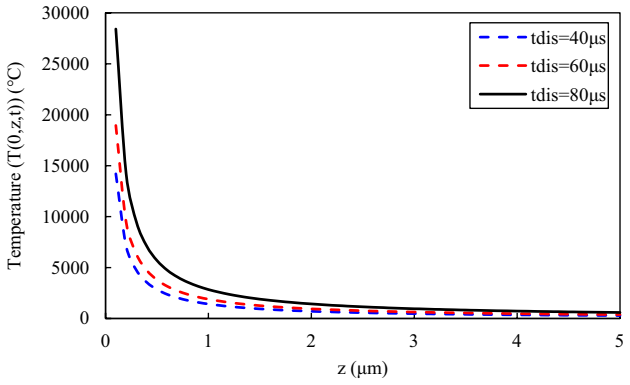

Fig. 9 Microcrater temperature distribution as a function of the microcrater depth

table. In addition, Fig. 9 shows the microcrater temperature distribution as a function of the microcrater depth. Notably, the temperature decreased exponentially with increasing microcrater depth. Also, an increase in t_{dis} increased the temperature for every microcrater-depth studied.

2.2.2 Cutting Force in HF-EDAM

Figure 10 shows the Merchant's model of cutting forces. Also, the cutting force in HF-EDAM (considering the influence of EDM on the material parameters of Ti6Al4V) can be solved by combining the temperature after discharge with the Johnson–Cook constitutive model of Ti6Al4V into the cutting force model of HF-EDAM. Further, the radial position angle of the cutting edge element in the HF-EDAM tool is denoted as $\varphi(t, z)$, where z is axial height of cutting edge element. And $k(t, z)$ denotes the axial position angle of the cutting edge element in the HF-EDAM tool, which is the angle between the tangential direction at the tool tip and the feeding direction. Since the helix angle of the shoulder milling cutter used is 0°, the axial position angle of the cutting edge element was chosen as 90°. Specifically, the up-milling to machine Ti6Al4V has the angles of cutting entry and exit, φ_{en} and φ_{ex}, respectively, determined by the following equation at a specific radial depth of cut a_e.

$$\begin{cases} \varphi_{en} = \frac{3\pi}{2} \\ \varphi_{ex} = \cos^{-1}\left(\frac{r_1 - a_e}{r_1}\right) + \varphi_{en} \end{cases} \tag{18}$$

In particular, since the axial depths of cut used in micro milling are small, this research developed a two-dimensional cutting force model of HF-EDAM, the axis cutting force dF_a is negligible, thus axial height of cutting edge element z is constant. Meanwhile, the two-dimensional cutting force model of CM has the micro-element tangential and radial cutting forces on the cutting edge, dF_t and dF_r, respectively, determined by the following equation.

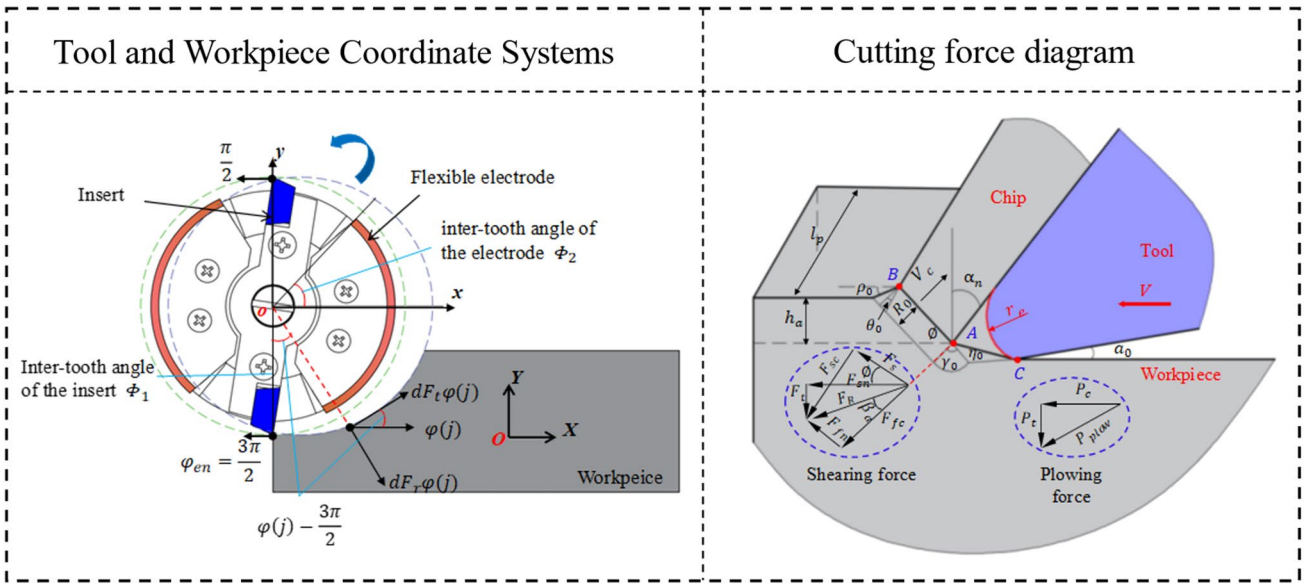

Fig. 10 Merchant's model of cutting forces

$$\begin{cases} dF_t(t,z) = K_{tc}h_a(t,z)db + K_{te}db \\ dF_r(t,z) = K_{rc}h_a(t,z)db + K_{re}db \end{cases} \tag{19}$$

where K_{tc} and K_{rc} are the tangential and radial shear force coefficients, and K_{te} and K_{re} are the tangential and radial ploughing force coefficients, respectively. The ploughing force coefficient can be calculated and determined by Eq. (22). In addition, h_a is the instantaneous undeformed chip thickness of the cutting edge element, with $h_a = f_z \cdot \sin\varphi \cdot \sin k$, where f_z is the feed per tooth. Finally, db is the cutting width of the cutting edge element, with $db = dz/\sin k$.

Converting the micro-element tangential and radial cutting forces on the cutting edge to the workpiece coordinate system OXY gives the following expression.

$$\begin{bmatrix} dF_X(t,z) \\ dF_Y(t,z) \end{bmatrix} = \begin{bmatrix} cos(\varphi(j) - \varphi_{en}) & \sin(\varphi(j) - \varphi_{en}) \\ sin(\varphi(j) - \varphi_{en}) & -cos(\varphi(j) - \varphi_{en}) \end{bmatrix} \begin{bmatrix} dF_t(t,z) \\ dF_r(t,z) \end{bmatrix} \tag{20}$$

where dF_X and dF_Y are the micro-element cutting forces on the cutting edge, along the X and Y directions, respectively. Subsequently, the micro-element cutting forces of all cutting edges participating simultaneously in cutting with a respective axial depth of cut of $[0, a_p]$ can be summed to get the two-dimensional cutting forces in the X and Y directions, F_X and F_Y, respectively, as follows.

$$\begin{cases} F_X(t) = \int_0^{a_p} dF_X(t,z) \\ F_Y(t) = \int_0^{a_p} dF_Y(t,z) \end{cases} \tag{21}$$

According to the classic bevel cutting model proposed by Armarego and Brown [24], K_{tc} and K_{rc} are determined by the following equation.

$$\begin{cases} \mathrm{K_{tc}} = \frac{\tau_s}{sin} \frac{cos(\beta_a - \alpha_n)}{\varnothing_n cos(\varnothing_n + \beta_a - \alpha_n)} \\ \mathrm{K_{rc}} = \frac{\tau_s}{sin\varnothing_n} \frac{sin(\beta_a - \alpha_n)}{cos(\varnothing_n + \beta_a - \alpha_n)} \end{cases} \tag{22}$$

where τ_s is the shear flow stress on the main shear plane, closely related to the cutting temperature and the key breakthrough aspect of the HF-EDAM cutting force model. Also, β_a, α_n, and $\varnothing_n$ are the friction, rake, and shear angles on the micro-element normal plane of the cutting edge, respectively. The friction angle is the correlation function of the cutting speed and friction coefficient, $\beta_a = \tan^{-1}(f_0 V^P)$, with the selected values in this research of $f_0 = 0.704$ and $P = -0.248$, and the cutting speed $V = 2\pi r_2 N$ [25], where N is spindle speed.

Subsequently, the rake angle on the micro-element normal plane of the cutting edge is replaced by the effective rake angle on the micro-element normal plane of the cutting edge, α_e, according to the average rake angle model proposed by Manjunathaiah [26]. So, the effective rake angle on the micro-element normal plane of the cutting edge can be calculated as:

$$\alpha_e = \begin{cases} \tan^{-1}\left(-\frac{\sqrt{\left(2 - \frac{\zeta h_a}{r_e}\right)\left(\frac{\zeta h_a}{r_e}\right)} - sin\theta_f}{\frac{\zeta h_a}{r_e} + cos\theta_f - 1} \right), \frac{h_a}{r_e} \le 1 + sin\alpha_0 \\ \tan^{-1}\left(\frac{\left(\frac{\zeta h_a}{r_e} - 1\right) tana_0 - \sec a_0 + sin\theta_f}{\frac{\zeta h_a}{r_e} + cos\theta_f - 1} \right), \frac{h_a}{r_e} > 1 + sin\alpha_0 \end{cases} \tag{23}$$

where r_e is the radius of the cutting edge of the tool, and α_0 is the nominal rake angle of the tool. And ζ is an empirical constant, generally taking the value 2. Finally, θ_f is the separation angle between the tool and the chip, taken as 37.6° in this research.

Further, the shear angle model proposed by Merchant can be used to approximate the shear angle on the micro-element normal plane of the cutting edge [27]:

$$\varnothing_n = \frac{\pi}{4} + \frac{\alpha_n}{2} - \frac{\beta_a}{2}. \tag{24}$$

Likewise, the slip line field model proposed by Waldorf [28] can be used to determine the tangential and radial ploughing force coefficients as follows.

$$\mathrm{K_{te}} = \left(\sigma_p \sin(\varnothing_n + \eta_0 - \gamma_0\right) + \tau_p cos(\varnothing_n + \eta_0 - \gamma_0))l_p$$

$$\mathrm{K_{re}} = \left(\sigma_p \cos(\varnothing_n + \eta_0 - \gamma_0\right) - \tau_p sin(\varnothing_n + \eta_0 - \gamma_0))l_p \tag{25}$$

where σ_p and τ_p are the normal and shear stresses on the micro-element ploughing surface of the cutting edge, respectively, and can be solved by the following equation. In addition, η_0 and γ_0 are the sector angles in the slip line field model, $\eta_0 = \frac{1}{2}\cos^{-1}(\mu_0)$, $\gamma_0 = \eta_0 + \varnothing_n - \sin^{-1}(\sqrt{2} sin\rho_0 sin\eta_0)$, and μ_0 was taken as 0.8 in this research. Relatedly, ρ_0 is another sector angle in the slip line field model. Finally, l_p is the length of the plow section, $l_p = R_0/\sin\eta_0$. $\mathrm{R_0}$ is the sector radius, which can be determined by Eq. (27). Meanwhile,

$$\begin{cases} \sigma_p = \tau_s(1 + 2\theta_0 + 2\gamma_0 + sin(2\eta_0)) \\ \tau_p = \tau_s cos(2\eta_0) \end{cases} \tag{26}$$

where $\theta_0 = \frac{\pi}{4} - \rho_0 - \varnothing_n$ is the bow angle, and its selected value was 10° in this research. Also,

$$R_0 = sin\eta_0 \sqrt{\left[r_e \times tan\left(\frac{\pi}{4} + \frac{\alpha_n}{2}\right) + \frac{\sqrt{2} R_0 sin\rho_0}{\frac{\pi}{4} + \frac{\alpha_n}{2}} \right]^2 + 2(R_0 sin\rho_0)^2}. \tag{27}$$

The shear flow stress on the main shear plane is affected by the preheating temperature of the spark discharge and temperature of heat generation by the plastic deformation during the cutting process. Therefore, the parameters in the Johnson–Cook constitutive model can be adjusted and

τ_s can be solved in combination with the spark temperature, T_{sl}. So,

$$\tau_s = \frac{1}{\sqrt{3}}(A + B\varepsilon^n)\left(1 + Cln\left(\frac{\dot{\varepsilon}}{\dot{\varepsilon}_0}\right)\right)\left((1 - \left(\frac{T_s - T_r}{T_m - T_r}\right)^m\right), \tag{28}$$

where A, B, C, m and n is the Johnson–Cook constitutive parameter of titanium alloys. For specific values, please refer to Table 3. where ε and $\dot{\varepsilon}$ are the equivalent stress and strain rates on the principal shear plane, respectively, and can be determined from Eq. (29) [29]. In addition, $\dot{\varepsilon}_0 = 1$, T_m is the melting point of the workpiece material, and T_s is the temperature of the main shear plane of the cutting edge element in HF-EDA. Subsequently, the non-bisected shear band model proposed by Tounsi [30] can be used to determine the temperature of the main shear plane of the cutting edge element in HF-EDAM as given in Eq. (30). Meanwhile,

$$\begin{cases} \varepsilon = \frac{c_0 cos\alpha_n}{\sqrt{3}cos(\varnothing_n - \alpha_n)sin\varnothing_n} \\ \dot{\varepsilon} = \frac{2Vcos\alpha_n}{\sqrt{3}t_a cos(\varnothing_n - \alpha_n)} \end{cases} \tag{29}$$

$$T_s = T_{sl} + \frac{c_0(2\tau_s + \tau_0)cos\alpha_n}{3\rho sin\varnothing_n cos(\varnothing_n - \alpha_n)}, \tag{30}$$

Table 3 Parameters used and their respective values for the cutting force prediction

Spindle speed (N)	3000 rpm
Feed rate (*f*)	10, 40, and 70 mm/min
Radial depth	0.15 mm
Axial depth	1.5 mm
Edge radius	0.005 mm
Helix angle	0°
Nominal rake angle	5°
Shear strength under quasi-static loading	480 MPa
Capacitances (C)	10,000, 100,000, and 1,000,000 pF
Voltage	220 V
A	905 MPa
B	835 MPa
C	0.028
n	0.28
m	1
T_m	1676 °C
T_r	25 °C

where c_0 is the non-equal division coefficient, which is calculated and determined by Eq. (31). Also, t_a is the thickness of the main shear zone, $t_a = h_a/2$. Finally, τ_0 is the initial pure shear yield strength of the workpiece material and can equal the material shear strength under quasi-static loading. Relatedly,

$$c_0 = \frac{1}{2} + \frac{\cos(2\varnothing_n - \alpha_n)}{2cos\alpha_n}. \tag{31}$$

The simultaneous Eqs. (28) and (31) can solve the shear flow stress on the main shear plane and the shear plane temperature T_s. Substituting the solved τ_s into Eqs. (18)–(27), the two-dimensional cutting force in HF-EDAM can be obtained.

After the HF-EDAM cutting force modeling, the distribution of cutting force for one revolution was predicted, i.e., with $\varphi \in [\pi, 3\pi]$. Table 3 gives the parameters used for the cutting force prediction. In addition, a comparison of the respective influence of different machining parameters on the cutting force was made by selecting three values of feed rate: 10, 40, and 70 mm/min. Finally, three different capacitances (10,000, 100,000, and 1,000,000 pF) were selected to find the respective effect of different discharge parameters on the cutting force.

Figure 11 shows the CM and HF-EDAM cutting forces predicted by modeling for the machining of Ti6Al4V. Notably, F_X is the cutting force in the feed direction. In addition, an increase in the feed rate increased the magnitude of the cutting force. At the same time, an increase in discharge time decreased the magnitude of the cutting force. Additionally, the feed rate of 10 mm/min had more cutting force drop rate after the HF-EDAM than that after the CM. This difference in cutting force drop rate was because the EDM assistance time is usually longer when the feed rate is lower.

2.3 The Experimental Equipment

Figure 12 shows the schematic HF-EADM system, which includes a simplified resistance-capacitor (RC)-transistor hybrid circuit, a three-axis micro-benchtop machine, a cutting force data collector, an oscilloscope, and a charge amplifier. The negative and positive poles of the EDM power supply are connected to the tool and workpiece, respectively. Notably, the discharge control RC-transistor hybrid pulse generator can charge and discharge normally even when the discharge gap is smaller than the normal discharge gap or when a short circuit occurs, as opposed to conventional discharge control RC pulse generators. Consequently, the discharge control RC-transistor hybrid pulse generator can make the charging and discharging voltage more regular, providing favorable conditions for a stable EDM.

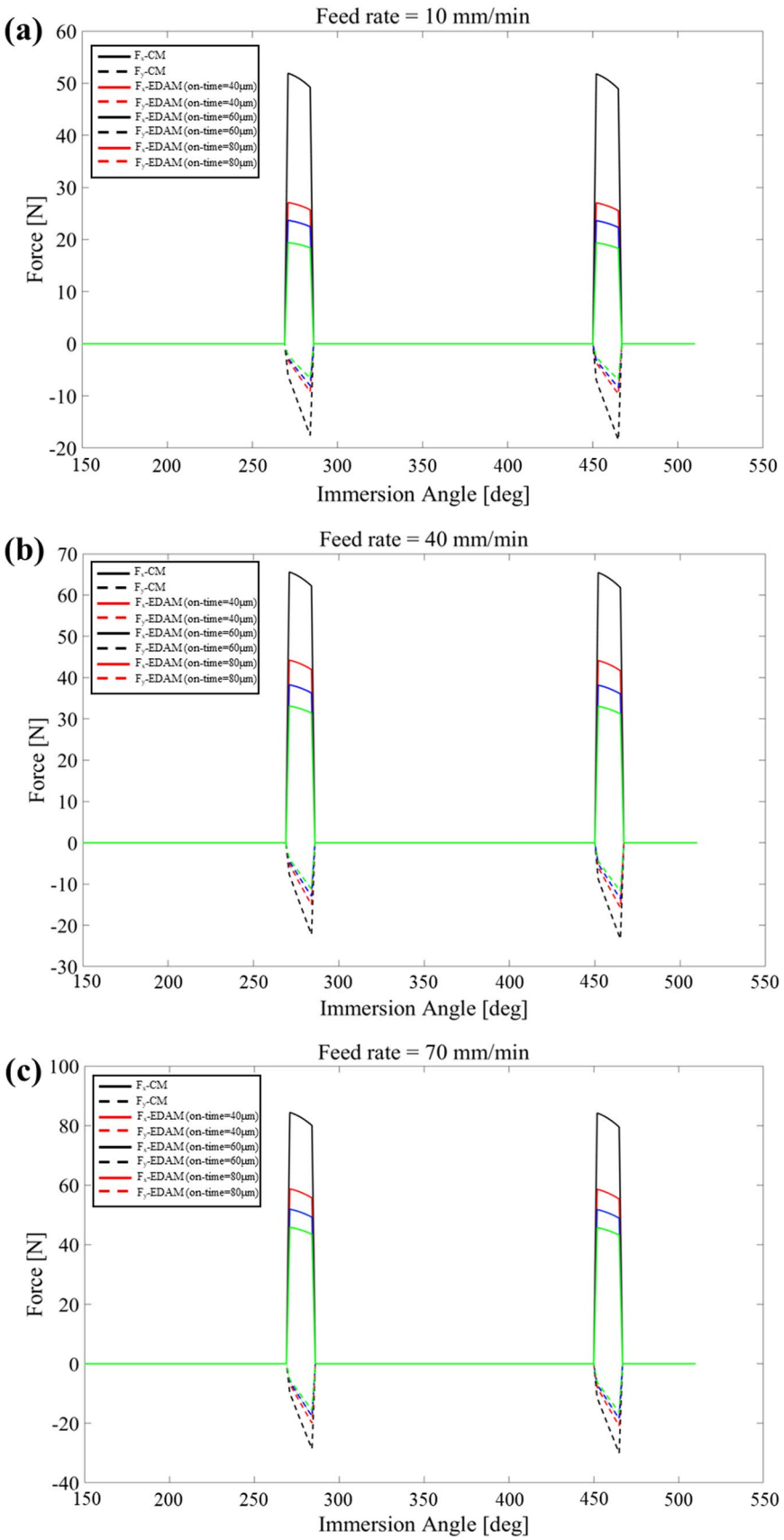

Fig. 11 The CM and HF-EDAM cutting forces predicted with a feed rate of: **a** 10, **b** 40, and **c** 70 mm/min, respectively, for the machining of Ti6Al4V

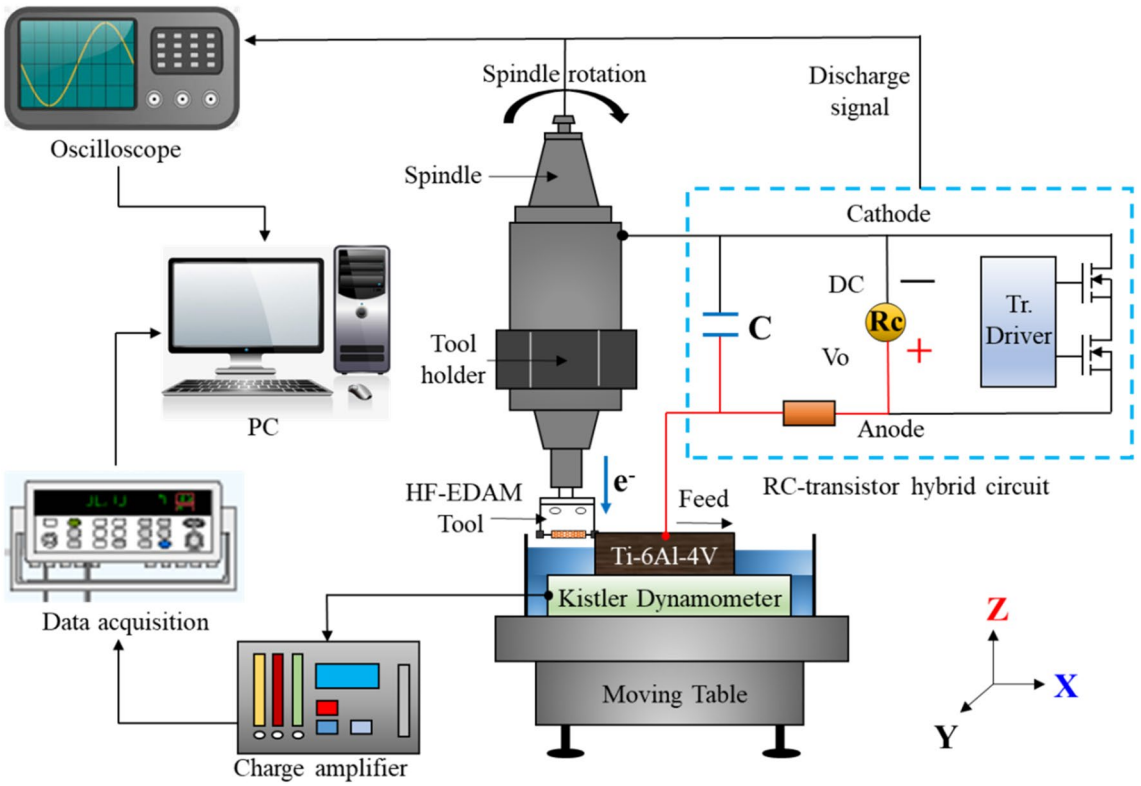

Fig. 12 Schematic HF-EDAM system

Figure 13 shows a photo of the HF-EDAM system and tool. The HF-EDAM tool was designed and manufactured specially. The tool is divided into three parts: (from left to right) the handle, plastic insulator, and tool holder. The plastic insulator is used to connect the tool handle and holder so that they are not energized. Moreover, one end of the tool holder is fixed on the spindle of the machine tool and connected to the EDM power supply, and the other end is used to fix the copper foam flexible electrode for EDM. Functionally, the tool holder is used to fix the milling insert.

Since the plastic insulator is in between the handle and tool holder, the spark current on the tool holder will not

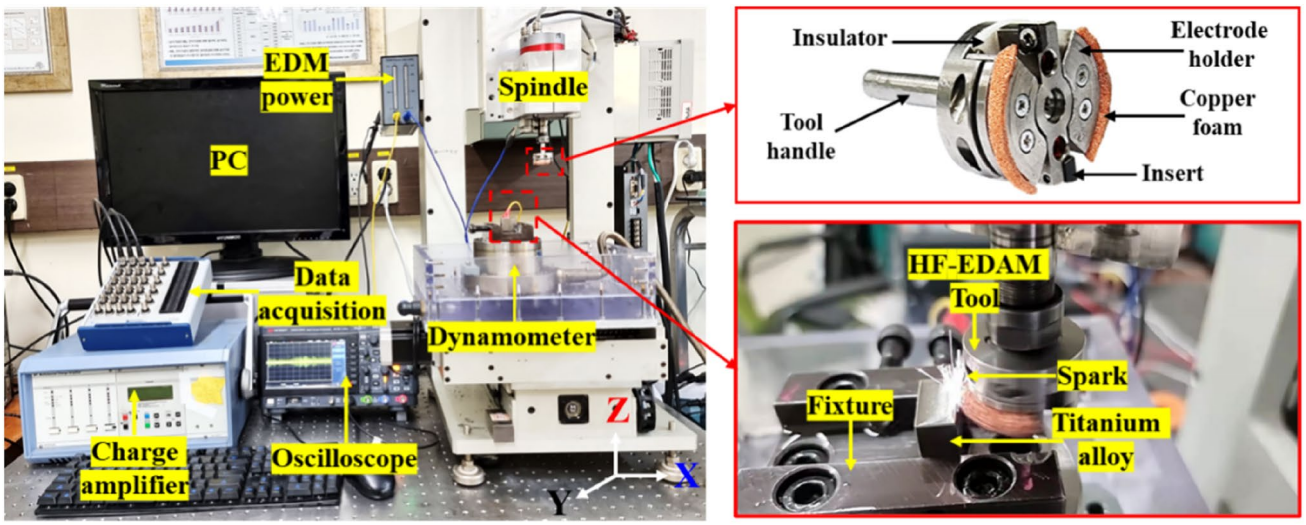

Fig. 13 The HF-EDAM system and tool

Table 4 Chemical composition of Ti6Al4V (%) [32]

H	N	C	O	Fe	V	Al	Ti
0.0053	0.01	0.02	0.18	0.22	4.02	6.08	89.464

Table 5 Physical and mechanical properties of Ti6Al4V [33]

Physical/mechanical property	Value
Modulus of elasticity	113 GPa
Melting point	1660 °C
Density	4.43 g/cm^3
Electrical resistivity	178 μΩ cm
Thermal conductivity	6.7 W/m/K
Vickers hardness	330–340 HV
Yield strength	835 MPa
Tensile strength	905 MPa
Poisson's ratio	0.33

discharge the milling insert, greatly increasing the tool life. Generally, copper electrodes and inserts can be fixed with ordinary steel bolts without insulation treatment. At the same time, the bottom screw can adjust the fastening of the copper foam flexible electrode to control the radial depth of the electrode. Compared to the previous EDAM tool [15], the HF-EDAM tool had a huge improvement in design, making up for many shortcomings in the machining.

Tables 4 and 5 give the chemical composition, and the physical and mechanical properties of Ti6Al4V, respectively. Meanwhile, the yield strength of a titanium alloy is about 1000 MPa higher, but its tensile strength decreases to 500 MPa at high temperatures [31]. Finally, the effect of metallurgical changes on the machined-material surface integrity was avoided by conducting experiments using the same batch of Ti6Al4V samples.

The parameters used during the experiment are shown in Table 6. Notably, the effect of different discharge energies on the experimental results was studied by choosing three different capacitances (10,000, 100,000, and 1,000,000 pF). Further, the RC-transistor hybrid circuit specifies $T_{\mathrm{on-time}}$ or the time to turn on the transistor within its usage range of 3–5 μs. In particular, the experiments of this study chose $T_{\mathrm{on-time}}$ as 4 μs. Likewise, $T_{\mathrm{off-time}}$ of the RC-transistor hybrid circuit is the turn-off time of the transistor. Generally, an experiment requires enough $T_{\mathrm{off-time}}$ to charge the capacitor. The usage range of $T_{\mathrm{off-time}}$ is usually 0.5–3 times the time constant T. Relatedly, the time constant varies with the resistance and capacitance according to,

$$T(s) = R(\Omega) \times C(F). \tag{32}$$

In addition, the resistance of the RC-transistor hybrid circuit was chosen as 1 kΩ in this study. Accordingly, calculations show that $T_{\mathrm{off-time}}$ has a range of 5–30, 50–300, and 500–3000 μs when the capacitance is 10,000, 100,000, and 1,000,000 pF, respectively. Hence, this study chose a $T_{\mathrm{off-time}}$ of 20, 200, and 2000 μs corresponding to the three capacitances. Likewise, the influence of different machining parameters on the experimental results was studied by choosing three different feed rates (10, 40, and 70 mm/min).

Further, the surface morphologies of the machined workpiece were studied using a 3D optical surface profiling device (NV-2000). Likewise, in order to check the detailed surface after machining, SEM (S-4800, HITACHI) was used. Additionally, energy dispersive spectroscopy (EDS) associated with SEM was used to study the respective species and amounts of elements present on the HF-EDAM-machined-material surface. Also, the high-speed camera used in the experiment was a Phantom miro C110. The phases present on the machined-material surface were then studied using an X-ray Powder Diffraction

Table 6 Experimental parameters of Ti6Al4V machining

	Experimental parameter	Unit	Values
Milling conditions	Method of milling		CM and HF-EDAM
	Spindle speed (N)	rpm	3000
	Feed rate (*f*)	mm/min	10, 40, and 70
	Radial depth	mm	0.15
	Axial depth	mm	1.5
EDM conditions	Capacitance (C)	pF	10,000, 100,000, and 1,000,000
	Voltage	V	220
	On-time	μs	4
	Off-time	μs	20, 200, and 2000
	Pulse generator type		RC-Transistor

(XRD) machine. Finally, the surface hardness (HV) of the machined material was measured using a microhardness tester (MMT-X7B, Matsuzawa). In particular, the accuracy of the measurement was improved by conducting three microhardness measurements at different places on the machined-material surface, and the average of the three measured hardnesses was taken as the machined-material surface microhardness.

3 Results and Discussion

3.1 Cutting Force and Tool Wear

Figure 14 shows the cutting force in CM and HF-EDAM of Ti6Al4V, respectively. In particular, the cutting force components (Fx, Fy, and Fz) and their resultant (Fr) are given in Fig. 14. Notably, the noise interference from the chatter of the machine tool to the cutting force measurement was reduced by using a filter method. Further, the cutting force measurement accuracy was improved by measuring the cutting force under each parameter three times, and the average of the three measured cutting forces was taken as the cutting force.

Particularly, the cutting force measurement was carried out for three different feed rates ($f = 10$, 40, and 70 mm/min), the intermediate capacitance 100,000 pF, and a spindle speed of 3000 rpm. The measured cutting forces in CM and HF-EDAM of Ti6Al4V, respectively, were then analyzed and compared. Figures 14 (a1), (b1), (c1), and (d1) show that as the feed rate increased, the cutting force components and resultant cutting force increased. This correlation is because the shear velocity in the shear plane increases with the feed rate, resulting in a concomitant increase in the shear force during machining. In addition, the increase in feed rate also increases the cutting amount per tooth so that the transient cutting area increases and the cutting force increases gradually.

In particular, the cutting force in HF-EDAM of Ti6Al4V was smaller than that in the CM due to the EDM assistance in HF-EDAM. This difference in cutting forces was more for lower feed rates. Further, this higher cutting force reduction at lower feed rates is because lower feed rates have a longer time of the EDM in HF-EDAM.

Figure 14 (a2), (b2), (c2), and (d2) show the cutting force waveform of CM and HF-EDAM of Ti6Al4V, respectively, for a feed rate of 10 mm/min. Meanwhile, the cutting force measurement error was reduced by starting the cutting process of the machining only after the measurement signal was stable. Also, the cutting force was measured first in the CM, and subsequently, the EDM power was turned on for the HF-EDAM when the same milling reached the middle position of the workpiece, and the corresponding cutting force was measured. Further, the cutting force waveforms show that the sinusoidal cutting force in the CM fluctuated more violently than that in the HF-EDAM.

Figure 15 shows the experimental and theoretical (model predicted) cutting forces in CM and HF-EDAM of Ti6Al4V for a capacitance of 100,000 pF. Meanwhile, the cutting force measurement accuracy was also improved by performing an analysis of the cutting force waveform by using the root mean square method to keep the waveform fluctuations within acceptable limits. Figure 15 also shows that the experimental and theoretical cutting forces were generally consistent. However, as the feed rate increased, the error between the theoretical and experimental cutting forces increased. This correlation can be attributed to disregarding the vibration and noise of the machine tool in the cutting force modeling.

Meanwhile, the tool wear in CM and HF-EDAM (for a capacitance of 100,000 pF) of Ti6Al4V, respectively, was studied after different lengths of machining for a feed rate of 10 mm/min. Figure 16 shows that an increase in the machining length made the tool wear in CM relative to HF-EDAM of Ti6Al4V more severe. This increased severity is because the severe friction between Ti6Al4V and the cutting edge in the CM creates scratches on the cutting edge, and the consequent peeling of the cutting edge coating increases the radius of the blunt circle in the cutting edge. Next, the blunt cutting edge leads to severe mechanical interaction between the tool flank and the workpiece, leading to a rapid tool wear increase. In particular, a machining length of 4000 mm had the tool in the CM fracture, while the corresponding HF-EDAM tool could still be used normally.

3.2 Discharge Signal

Figure 17 shows the charging and discharging voltage signals of each plasma spark pulse in HF-EDAM. In particular, the total time required to generate a plasma spark in a charging-discharging cycle (T_p) includes the charging time (t_{ch}), idling time (t_{id}), and discharging time (t_{dh}):

$$T_p = t_{ch} + t_{id} + t_{dh}. \tag{33}$$

Also, each HF-EDAM discharge includes multiple charging and dischargings, so the total discharge time for N plasma spark pulses, T_{total}, is:

$$T_{total} = T_p \times N. \tag{34}$$

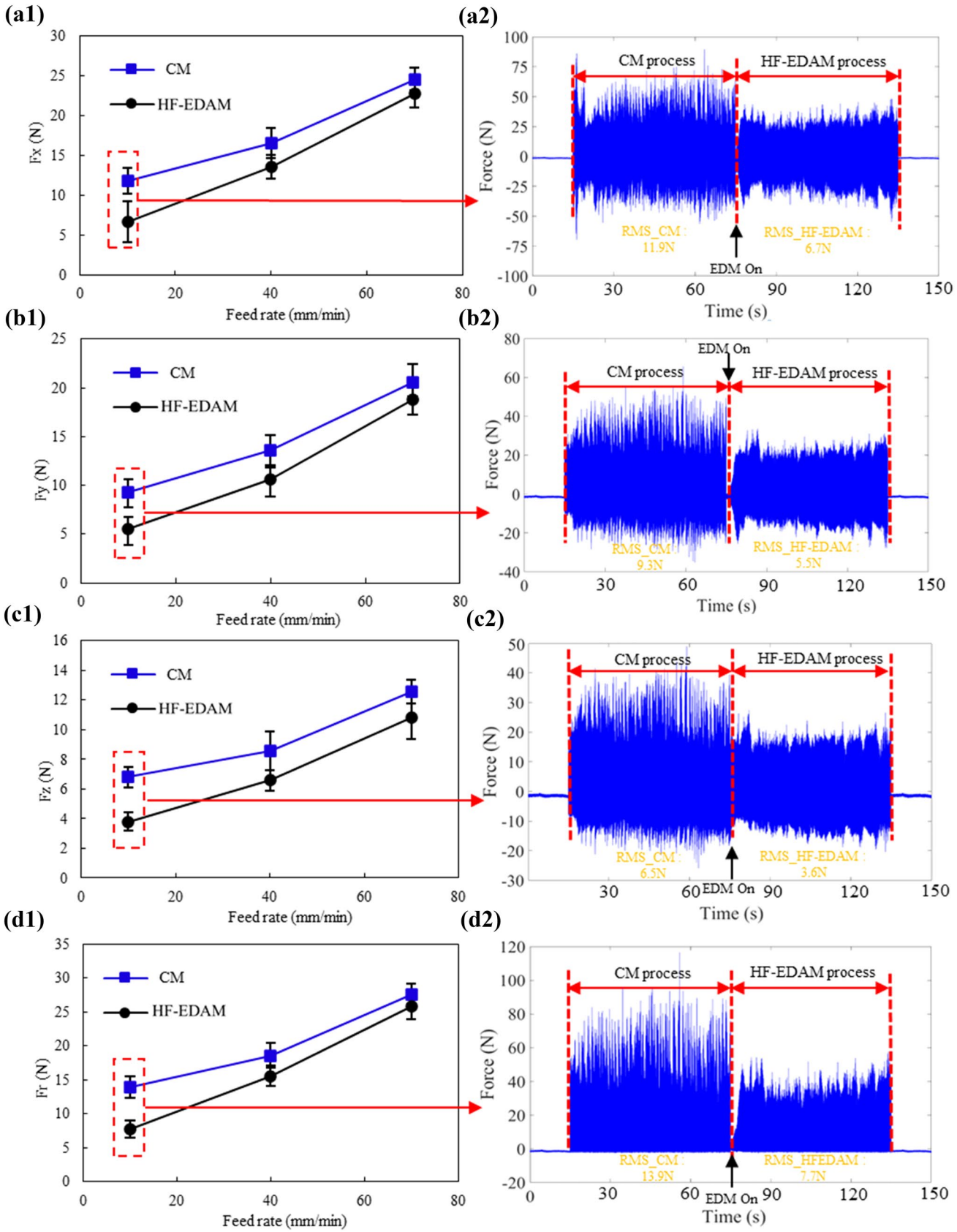
(a1)
CM
HF-EDAM
Fx (N)
Feed rate (mm/min)
(a2)
CM process
HF-EDAM process
Force (N)
RMS_CM : 11.9N
RMS_HF-EDAM : 6.7N
EDM On
Time (s)
(b1)
CM
HF-EDAM
Fy (N)
Feed rate (mm/min)
(b2)
EDM On
CM process
HF-EDAM process
Force (N)
RMS_CM : 9.3N
RMS_HF-EDAM : 5.5N
Time (s)
(c1)
CM
HF-EDAM
Fz (N)
Feed rate (mm/min)
(c2)
CM process
HF-EDAM process
Force (N)
RMS_CM : 6.5N
RMS_HF-EDAM : 3.6N
EDM On
Time (s)
(d1)
CM
HF-EDAM
Fr (N)
Feed rate (mm/min)
(d2)
CM process
HF-EDAM process
Force (N)
RMS_CM : 13.9N
RMS_HFEDAM : 7.7N
EDM On
Time (s)

◂**Fig. 14** Cutting force in CM and HF-EDAM of Ti6Al4V for a capacitance of 100,000 pF: **a1**, **b1**, **c1**, and **d1** show the variation of the cutting force components (F_X, F_Y, and F_Z) and resultant cutting force (F_r) with the feed rate; and **a2**, **b2**, **c2**, and **d2** show the waveform of cutting force components and resultant cutting force for a feed rate of 10 mm/min, respectively

In addition, several factors, such as the parameters $T_{\text{on-time}}$, $T_{\text{off-time}}$, and capacitance, affect the discharge frequency in HF-EDAM.

Further, the RC-transistor hybrid circuit in HF-EDAM has the relationship between the charging voltage (V_{ch}) and time of the capacitor as follows.

$$V_{ch} = 1 - e^{-\frac{t_{ch}}{T}}. \tag{35}$$

In particular, V_{ch} is the maximum voltage during the charging of the capacitor, and T is the time constant equal to the product of resistance and capacitance (RC). Subsequent to reaching the maximum voltage during the charging of the capacitor, idling occurs for the idling time. Finally, the discharging of the capacitor at the discharging voltage (V_{dh}) can be expressed as:

$$V_{dh} = e^{-\frac{t_{dh}}{T}}. \tag{36}$$

The EDM discharge voltage waveform measured in HF-EDAM for different capacitances by using an oscilloscope is shown in Fig. 18. Unlike in typical discharge voltage waveforms, the discharge and open-circuit states alternated in that of HF-EDAM. So, there is no charging and discharging of the capacitor in the RC-transistor hybrid circuit during the open-circuit state, and correspondingly there is no milling. Figure 18 shows that the interval between two discharges was 10 ms, consistent with the spindle speed of 3000 rpm (20 ms per revolution with two copper foam flexible electrodes) used in the experiment. Figure 18 also shows that the discharge time of the copper foam flexible electrode was about 5.5 ms for a capacitance of 100,000 pF, which is about five times that reported in the previous research [15].

Further comparisons with the previous research [15] showed that a capacitance of 10,000, 100,000, and 1,000,000 pF with off-time of 20, 200, and 2,000 µs in HF-EDAM resulted in 235, 23.5, and 2.35 times discharge time increase as compared to those reported in the previous research, respectively. However, a limitation on the acquisition rate of the oscilloscope led to the capture of only part of the discharge pulse signal in HF-EDAM for a capacitance of 10,000 pF.

3.3 Discharge Crater

The experiment found that the capacitance of the RC-transistor hybrid circuit in HF-EDAM affected the size of the crater on the workpiece after discharge (discharge crater). Figure 19 shows the discharge craters formed on Ti6Al4V after 3 turns of the copper foam flexible electrode for different capacitances (10,000, 100,000, and 1,000,000 pF). In particular, the discharge crater depth increased as the capacitance increased. However, the number of discharge craters reduced with increased capacitance, due to the longer off-time required for higher capacitances. An increase in the capacitance also made the crater distribution more dispersed. Also, a decrease in the capacitance made the craters overlap due to the increased number of discharge pulses.

Figure 20 shows a graph of a single discharge crater depth of Ti6Al4V after three turns of the copper foam flexible electrode for different capacitances. Notably, a comparison of these crater depths is helpful as a reference for the formulation of discharge parameters in the HF-EDAM process.

3.4 Surface Morphology of Electrode and Workpiece After the Machining

The morphological changes of the flexible electrodes and workpiece in HF-EDAM of Ti6Al4V were analyzed using the surface SEM images, and the same analysis in 3D was performed using a 3D optical surface profiler. Figure 21 shows the SEM and EDS images, and 3D topography of the copper foam flexible electrode before and after the machining, respectively, for a feed rate of 10 mm/min and capacitance of 100,000 pF. In particular, the SEM image of the copper foam flexible electrode before the machining shows the electrode having a network structure.

Scratches and molten workpiece material were also observed on the copper foam flexible electrode surface after the machining. Generally, scratches are formed on an electrode surface during machining because the electrode inevitably contacts the workpiece surface during the machining. However, the molten workpiece material was mostly distributed inside the flexible electrode.

Notably, the energy dispersive X-ray spectrometer (EDS) was used to study the change of elemental species and content of the copper foam flexible electrode before and after the machining, respectively. The EDS image of the copper foam flexible electrode before and after the machining, respectively, shows that the carbon (C) content on the electrode surface after the machining increased compared to that on the electrode surface before the machining, and Ti and Al

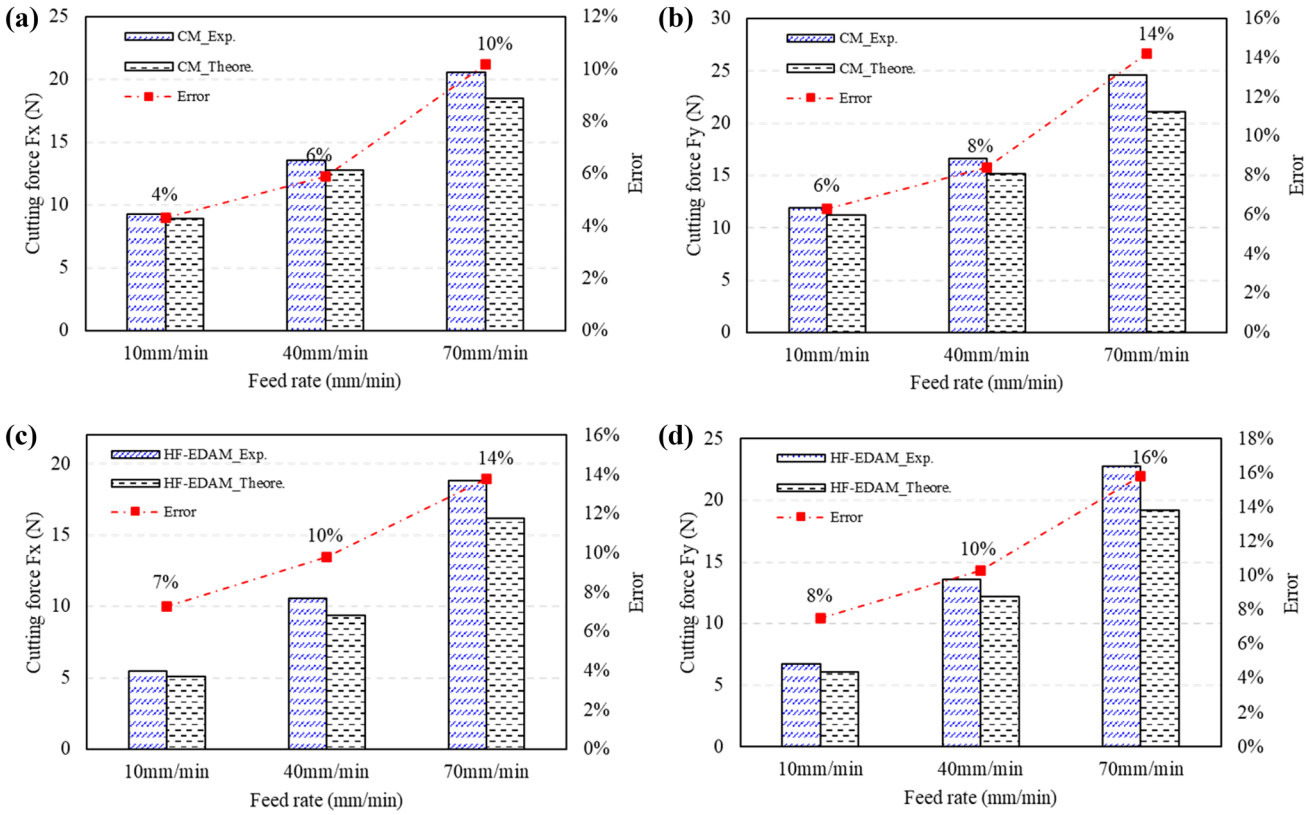

Fig. 15 Comparison between experimental and theoretical (model predicted) cutting forces for a capacitance of 100,000 pF: **a** and **b** X and Y direction cutting forces in CM of Ti6Al4V; and **c** and **d** X and Y direction cutting forces in HF-EDAM of Ti6Al4V, respectively

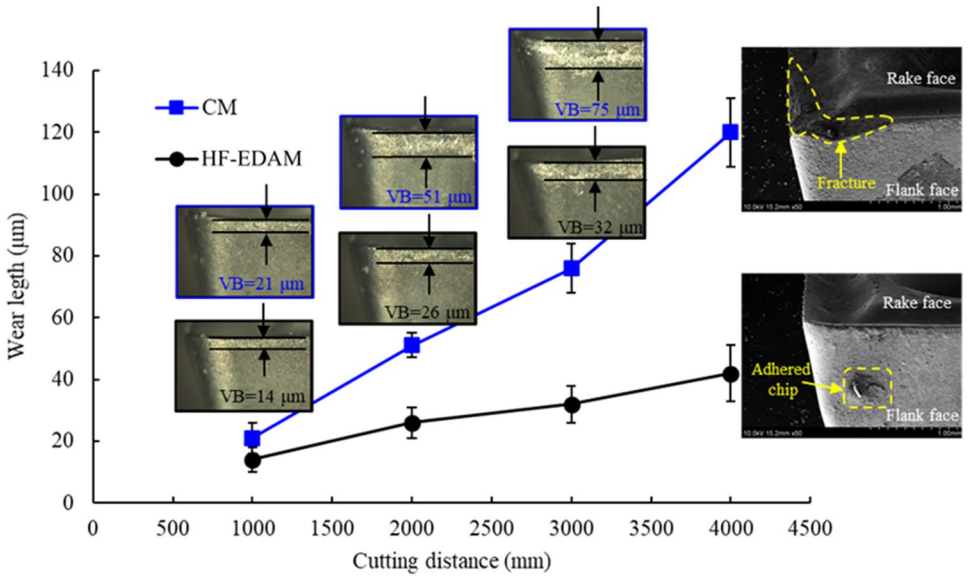

Fig. 16 Tool wear in CM and HF-EDAM (with a capacitance of 100,000 pF) of Ti6Al4V, respectively, after different lengths of machining for a feed rate of 10 mm/min

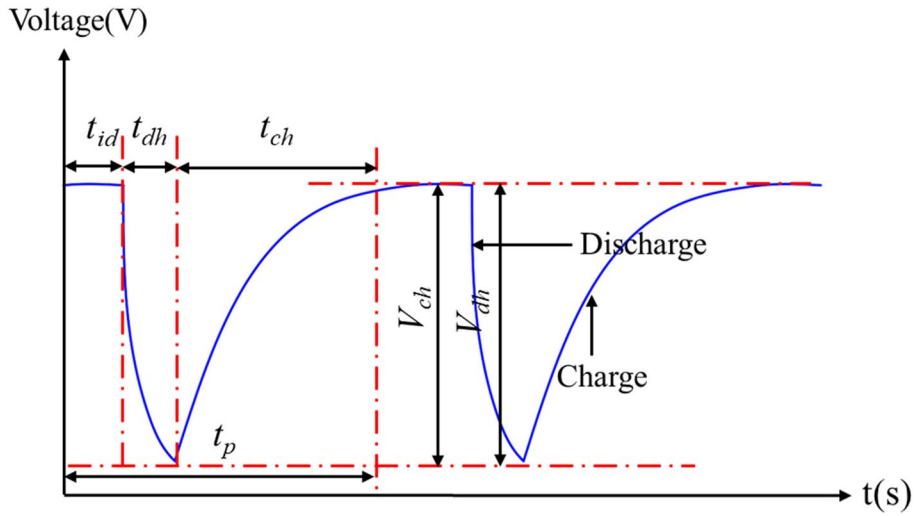

Fig. 17 Illustration of the charging and discharging voltage signals of each plasma spark pulse in HF-EDAM

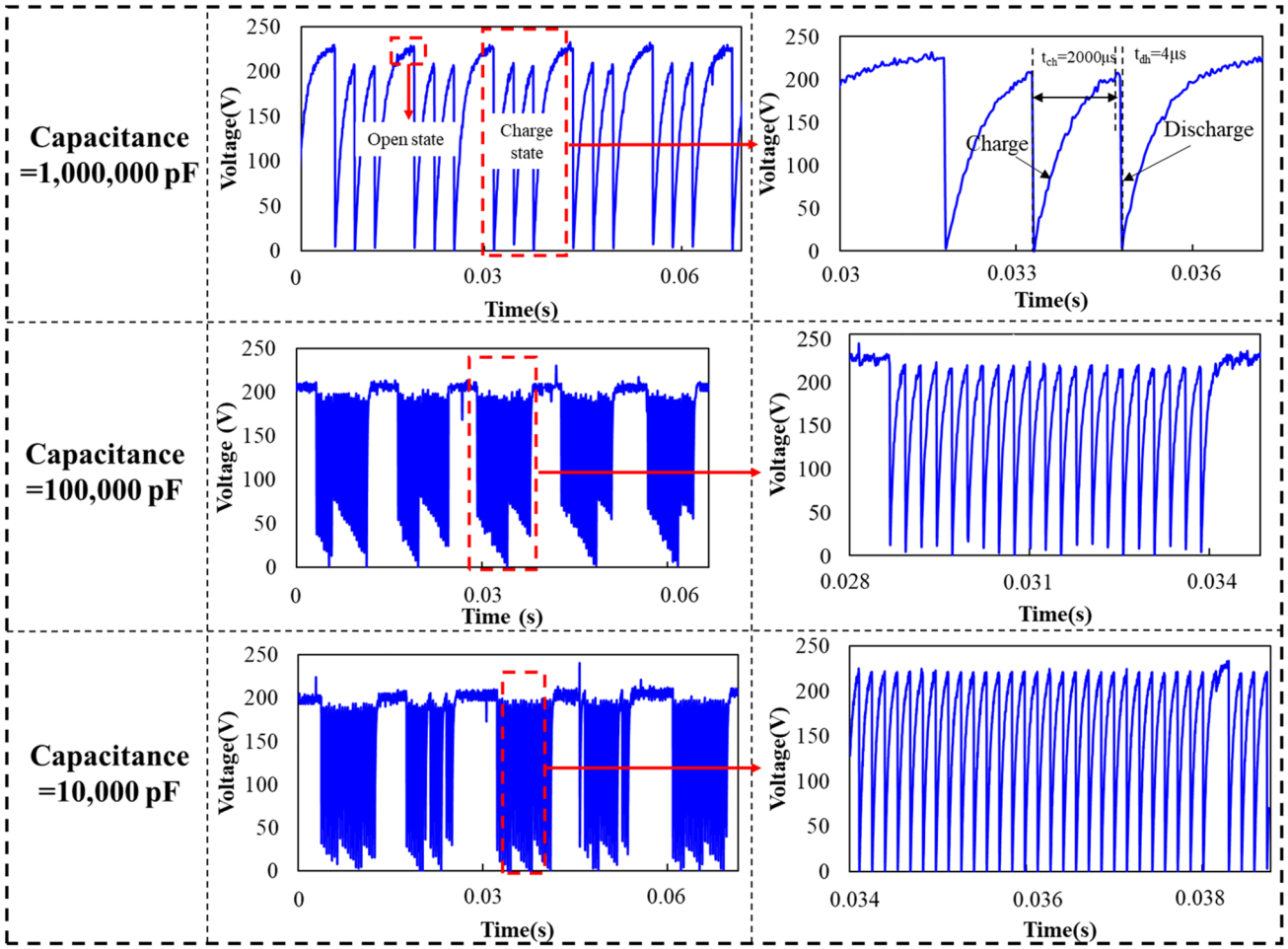

Fig. 18 EDM discharge voltage wave form in HF-EDAM for a capacitance of 10,000, 100,000, and 1,000,000 pF, respectively

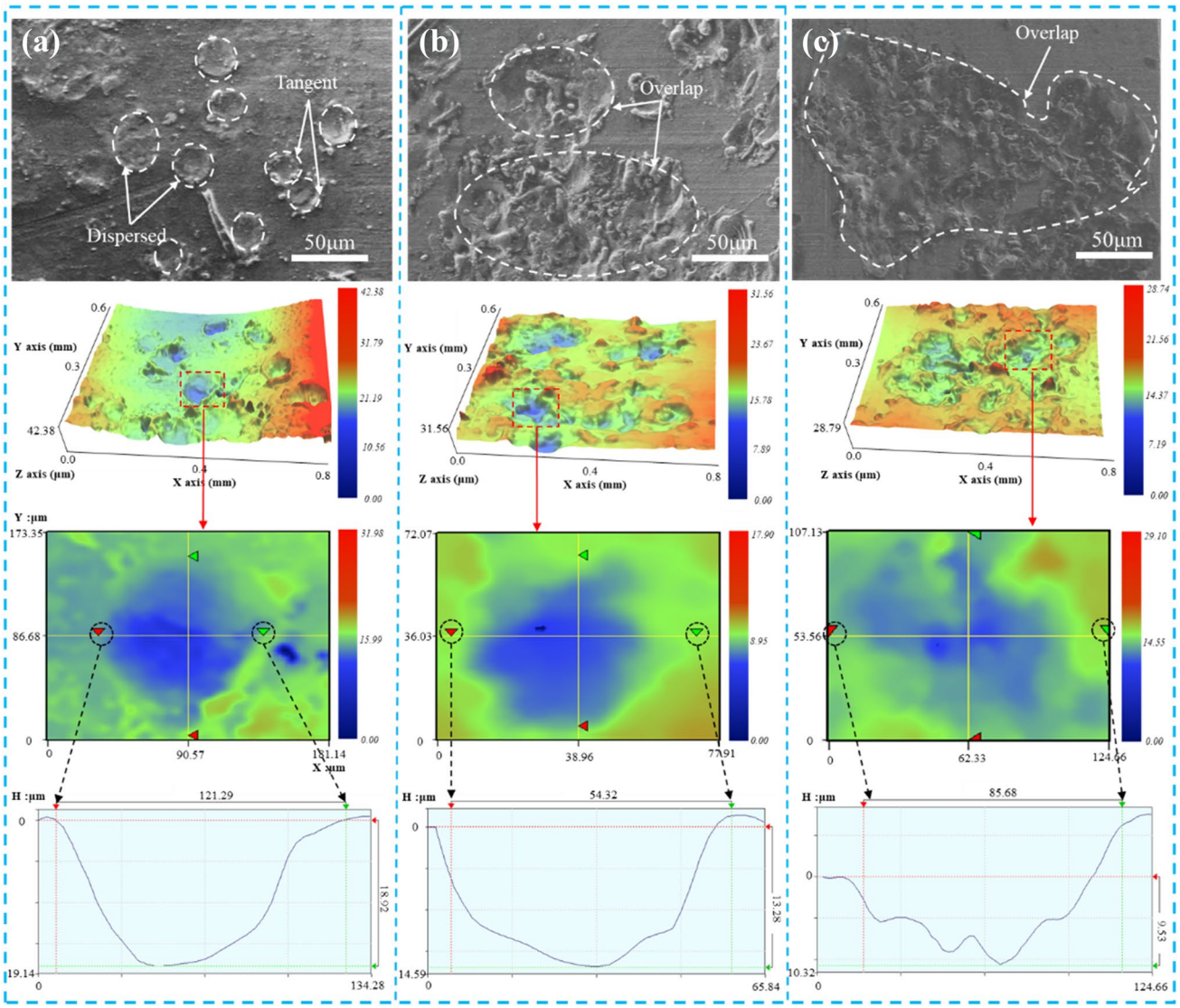

Fig. 19 SEM image and 3D topography of the discharge craters formed on Ti6Al4V after three turns of the copper foam flexible electrode and for a capacitance of: **a** 1,000,000 pF, **b** 100,000 pF, and **c** 10,000 pF, respectively

elements were generated during the machining. Such an increase in C content is normally due to the dielectric in HF-EDAM, and the discharge effect of the EDM in HF-EDAM also aggravates the penetration of the dielectric into the electrode surface. On the other hand, the generation of Ti and Al elements is normally caused by the contact between the electrode and the Ti6Al4V surface.

Figure 22 gives the SEM image, 3D topography, EDS image, and EDS maps of the machined-Ti6Al4V surface in CM of Ti6Al4V for a feed rate of 10 mm/min. Likewise, Fig. 23 gives the same details in HF-EDAM of Ti6Al4V for a feed rate and capacitance of 10 mm/min and 100,000 pF, respectively. Notably, the SEM image of the machined-Ti6Al4V surface in the CM shows that the surface defects included: adhered chips, debris, and feed marks. On the other hand, the surface defects of the machined Ti6Al4V in the HF-EDAM mainly included adhered chips, debris, and melt. In particular, adhered chips were the main reason for the high surface roughness of the corresponding machined Ti6Al4V.

Obviously, the chip adhesion in the CM was significantly greater than that in the HF-EDAM due to the greater heat

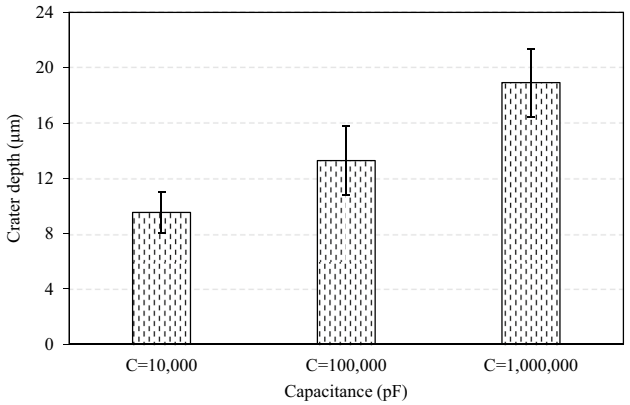

Fig. 20 A single discharge crater depth of Ti6Al4V after three turns of the copper foam flexible and for a capacitance of 10,000, 100,000, and 1,000,000 pF, respectively

generation in the CM. Also, the generation of melt in the HF-EDAM was by the EDM in the HF-EDAM, and the generated melt remained on the machined-Ti6Al4V surface. Importantly, there were obvious burrs on the edge of the machined-Ti6Al4V surface in the CM and not in the HF-EDAM.

The EDS image of the machined-Ti6Al4V surface in the CM and HF-EDAM, respectively, shows that the machined-Ti6Al4V surface elements in the CM mainly included Ti, Al, C, and V, and those in the HF-EDAM mainly included Ti, Al, C, and Cu. Generally, the Ti, V, and Al are from Ti6Al4V, and the C in the case of HF-EDAM is from the dielectric infiltration into Ti6Al4V. Further, the Cu is normally produced by the discharge between the copper foam flexible electrode and the workpiece (Ti6Al4V, in this study) during the EDM in HF-EDAM.

The EDS map of the machined-Ti6Al4V surface in the CM and HF-EDAM, respectively, shows that the surface was almost covered by Ti elements, and the V and Al contents were relatively low and overlapped each other. In addition, the C content was mainly distributed on the adhered chips on the machined-Ti6Al4V surface in both the CM and HF-EDAM. Also, Fig. 23 shows that a noticeable Cu element distribution was observed on the substrate of the machined-Ti6Al4V surface in the HF-EDAM. This Cu element distribution is normally because of the inevitable contact of the copper foam flexible electrode with the workpiece (Ti6Al4V, in this study) surface in HF-EDAM, and the remaining of the electrode surface Cu element on the machined-material surface when the spark discharges rapidly.

Figure 24 shows the machined-Ti6Al4V surface roughness in CM and HF-EDAM of Ti6Al4V, respectively, for different feed rates. Notably, the machined-Ti6Al4V surface roughness (Ra) in the HF-EDAM was lower than that in the CM. This difference in the surface roughnesses is normally due to the auxiliary action of the EDM in HF-EDAM effectively reducing the generation of cutting force and heat, thereby reducing excessive bonding of the workpiece (Ti6Al4V, in this study) and tool during chip formation. At the same time, the advantages of the HF-EDAM, in terms of the machined-Ti6Al4V surface roughness, were even greater for lower feed rates. These greater advantages are generally because of the longer EDM assistance time in HF-EDAM for lower feed rates.

3.5 Micro-hardness

This study measured the machined-Ti6Al4V surface hardness in CM and HF-EDAM (with a capacitance of 100,000 pF) of Ti6Al4V, respectively, for different feed rates by using the microhardness tester. In particular, the load applied by the indenter of the tester to the machined-Ti6Al4V surface was 200 g, and the load was held for the 10 s of the test.

Figure 25 shows that the machined-Ti6Al4V surface hardness increased with an increasing feed rate in the CM and HF-EDAM, respectively. However, the machined-Ti6Al4V surface hardness in the CM was greater than that in the HF-EDAM for every feed rate. This difference in the machined-Ti6Al4V surface hardnesses is mainly due to the strain hardening of Ti6Al4V with an increasing feed rate in the CM. At the same time, the EDM in the HF-EDAM reduces the cutting force and heat, thereby reducing the strain hardening to a certain extent.

3.6 Plastic Deformation

Figure 26 shows the machined-Ti6Al4V subsurface plastic deformation in CM and HF-EDAM (with a capacitance of 100,000 pF) of Ti6Al4V, respectively, for a feed rate of 40 mm/min. In particular, the β grains below the machined-Ti6Al4V surface were significantly deformed, and the direction of plastic deformation caused by the machining was rotated along the cutting direction in the CM. However, almost no plastic deformation was observed in the machined-Ti6Al4V subsurface in the HF-EDAM. Generally, the changes in a machined-material subsurface grain structure are inseparable from the changes in mechanical and thermal loads on the workpiece (Ti6Al4V, in this study) during cutting. Since the EDM in HF-EDAM softens the workpiece surface into a free-cutting layer (which is then removed by the milling process) to eventually reduce the cutting force, the corresponding smaller mechanical load

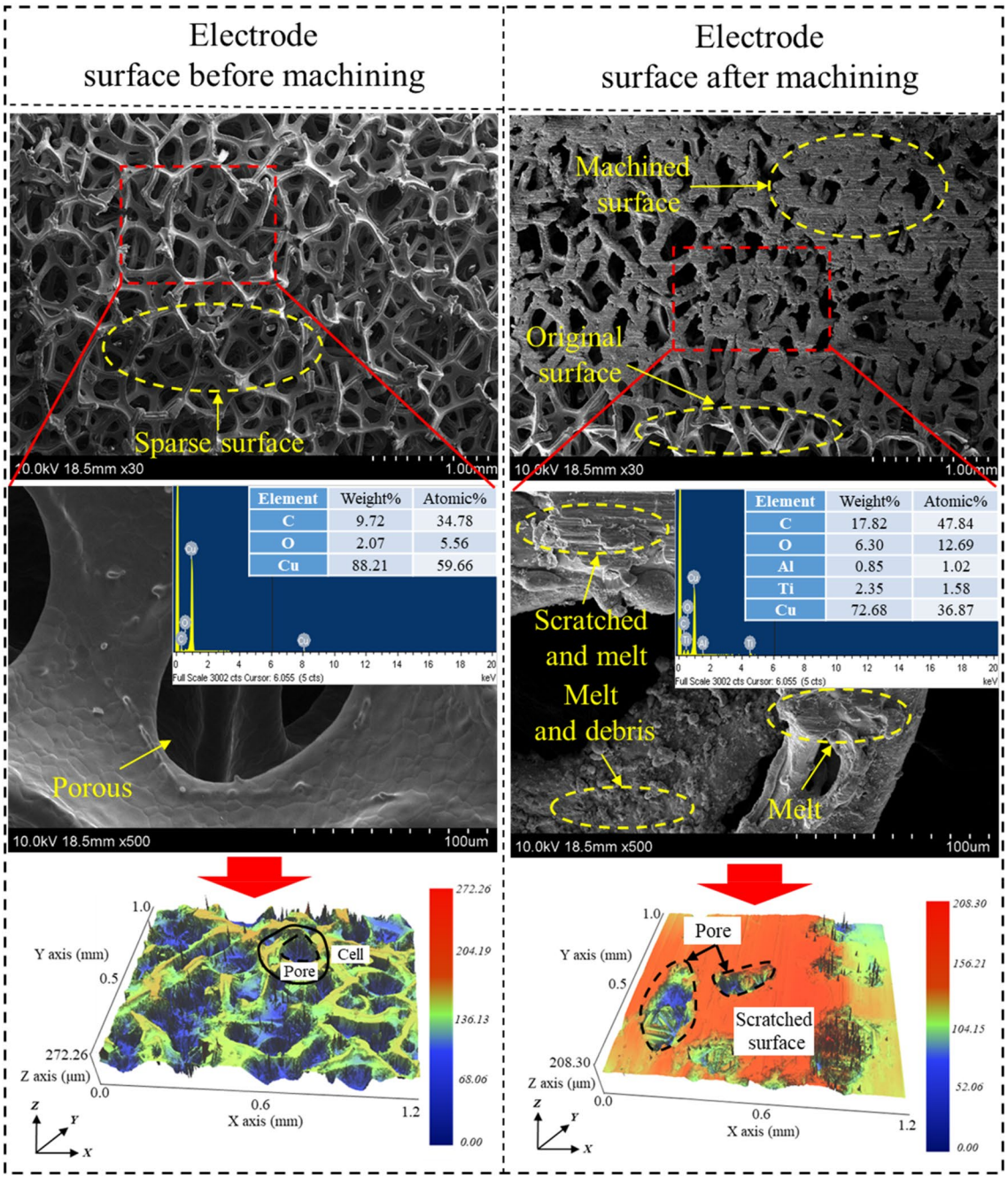

Fig. 21 SEM and EDS images (top and middle images, respectively), and 3D morphology (bottom image) of the copper foam flexible electrode before and after HF-EDAM of Ti6Al4V, respectively, for a feed rate of 10 mm/min and capacitance of 100,000 pF

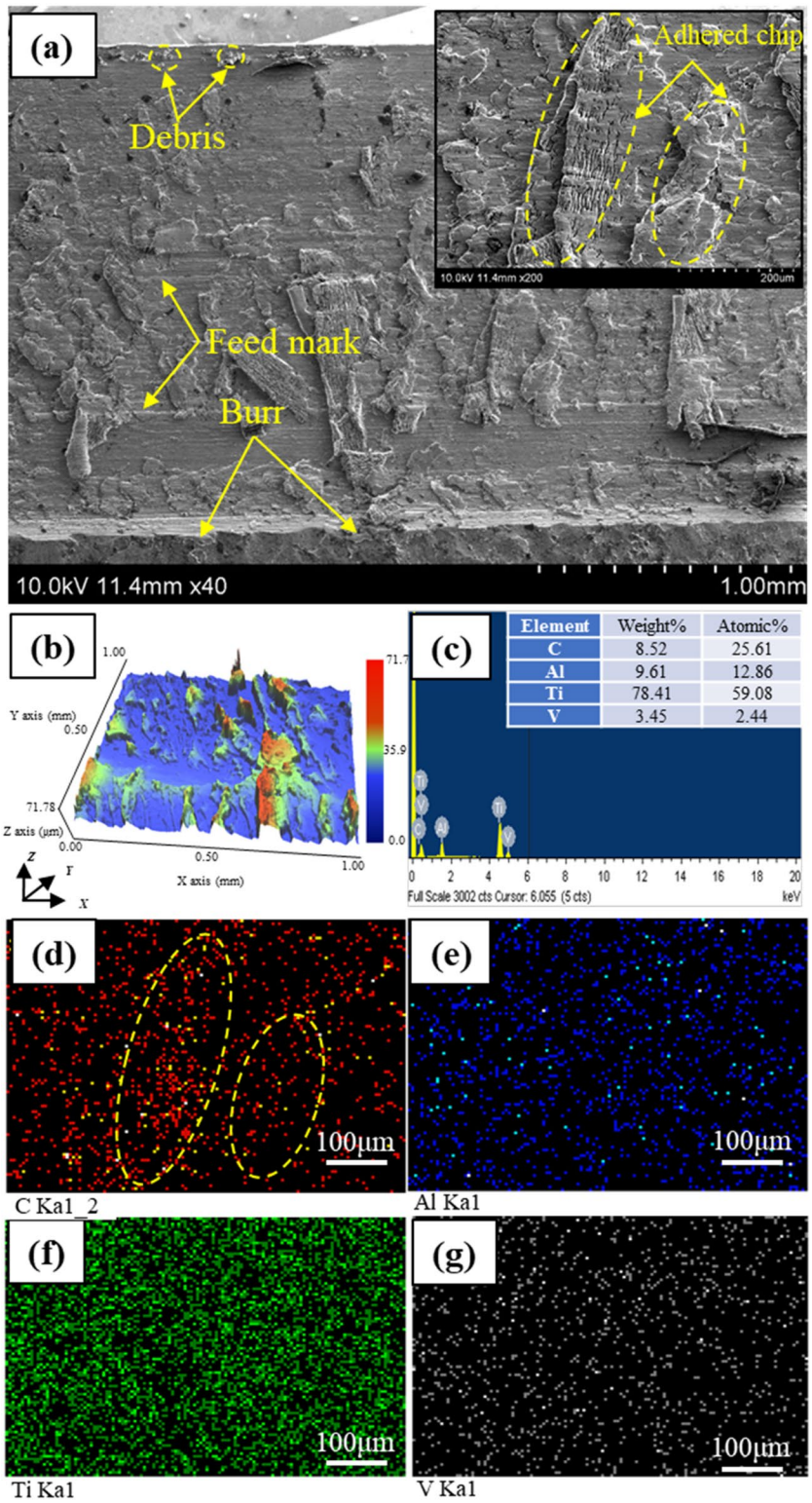

Fig. 22 Machined-Ti6Al4V surface in CM of Ti6Al4V for a feed rate of 10 mm/min: surface **a** SEM image; **b** 3D topography; **c** EDS image; **d** analogous elemental mapping of the C element; **e** analogous elemental mapping of the Al element; **f** analogous elemental mapping of the Ti element; and **g** analogous elemental mapping of the V element

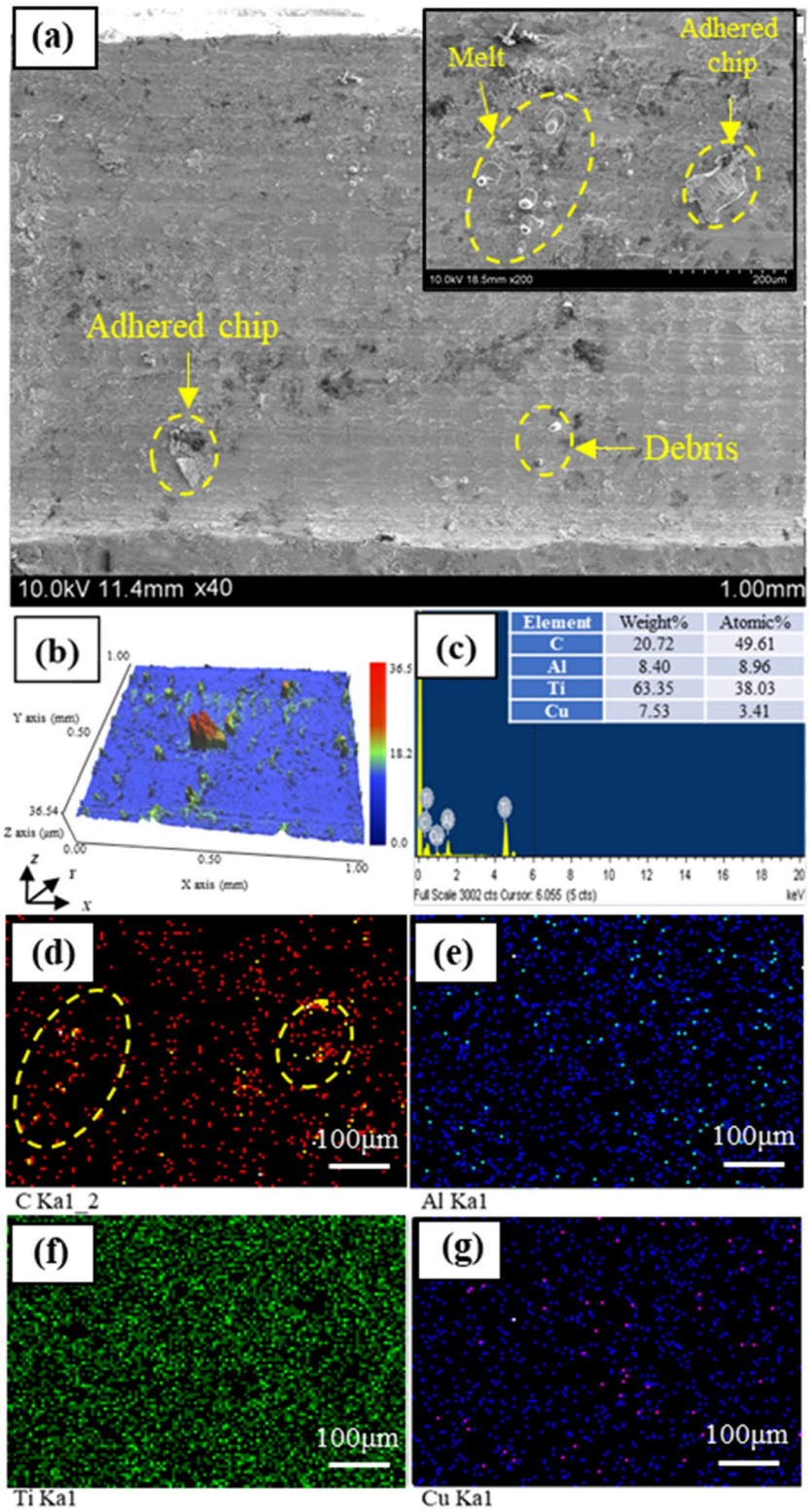

Fig. 23 Machined-Ti6Al4V surface in HF-EDAM of Ti6Al4V for a feed rate and capacitance of 10 mm/min and 100,000 pF, respectively: surface **a** SEM image; **b** 3D topography; **c** EDS image; **d** analogous elemental mapping of the C element; **e** analogous elemental mapping of the Al element; **f** analogous elemental mapping of the Ti element; and **g** analogous elemental mapping of the Cu element

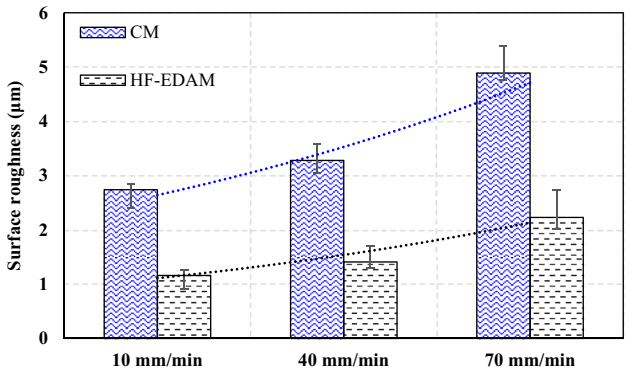

Fig. 24 Machined-Ti6Al4V surface roughness (Ra) in CM and HF-EDAM (with a capacitance of 100,000 pF) of Ti6Al4V, respectively, for a feed rate of 10 mm/min

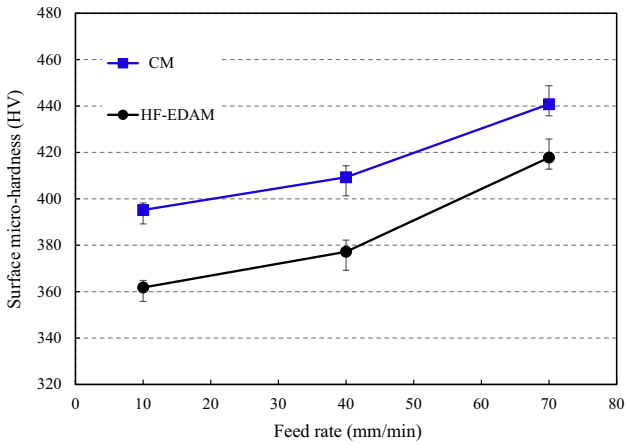

Fig. 25 Machined-Ti6Al4V surface hardness in CM and HF-EDAM (with a capacitance of 100,000 pF) of Ti6Al4V, respectively, for different feed rates

on the workpiece reduces the plastic layer thickness of the machined-material subsurface.

4 Conclusions

This article presented new hybrid machining, HF-EDAM (based on a novel tool with flexible electrodes). Meanwhile, the feasibility of machining Ti6Al4V by HF-EDAM was deeply studied through experiments and modeling, and the following conclusions were drawn from the study.

(1) The copper foam flexible electrode fitted perfectly with the HF-EDAM tool due to the unique flexibility and network structure of the electrode. So, the flexible electrode could effectively adjust its surface shape to match the workpiece surface in HF-EDAM, thereby achieving perfect discharge conditions. As a result, the flexible electrode effectively avoided the occurrence of short-circuit discharge during machining, and the discharge efficiency and time in the machining significantly improved compared to those reported in previous studies, respectively.

(2) The comparison of the discharge signal and crater under different capacitances between previous research that used an ordinary electrode and HF-EDAM showed that the discharge time in HF-EDAM, based on flexible electrodes, was 5 times that reported in the previous research. In addition, the larger the capacitance, the lesser the number of craters after discharge, and the more dispersed the distribution of craters was for any discharge time in HF-EDAM of Ti6Al4V.

(3) Comparing the cutting force and tool wear in different machining methods showed that an increase in the feed rate increased the cutting force in all the methods. In addition, lower feed rates had a more significant cutting force reduction effect in the HF-EDAM as compared to that in the CM. According to the measurement results, when the feed rate is 10 mm/min, compared with CM, the cutting force Fy in the feed direction after HF-EDAM is relatively decreased by 77.6%, and the total cutting force Fr after HF-EDAM is relatively decreased by 80.5%.

(4) Comparing the experimental measurements and model predictions of cutting force in the HF-EDAM showed that the theoretical (model predicted) cutting force was consistent with that of the experimentally measured one. Also, the cutting force in the HF-EDAM was effectively reduced compared to that in the CM. Hence, the high effectiveness of HF-EDAM in machining difficult-to-machine materials (Ti6Al4V, in this study) was theoretically demonstrated.

(5) The research on the machined-material surface integrity in different machining methods showed that the HF-EDAM could effectively improve the surface integrity as compared to those in the other methods. In addition, the reduction of cutting force in HF-EDAM led to a small plastic deformation layer thickness of the machined-material subsurface. Also, an increase in the feed rate increased the machined-material surface hardness in both the CM and HF-EDAM, and the surface hardness in the CM was greater than that in the HF-EDAM for all the conditions studied.

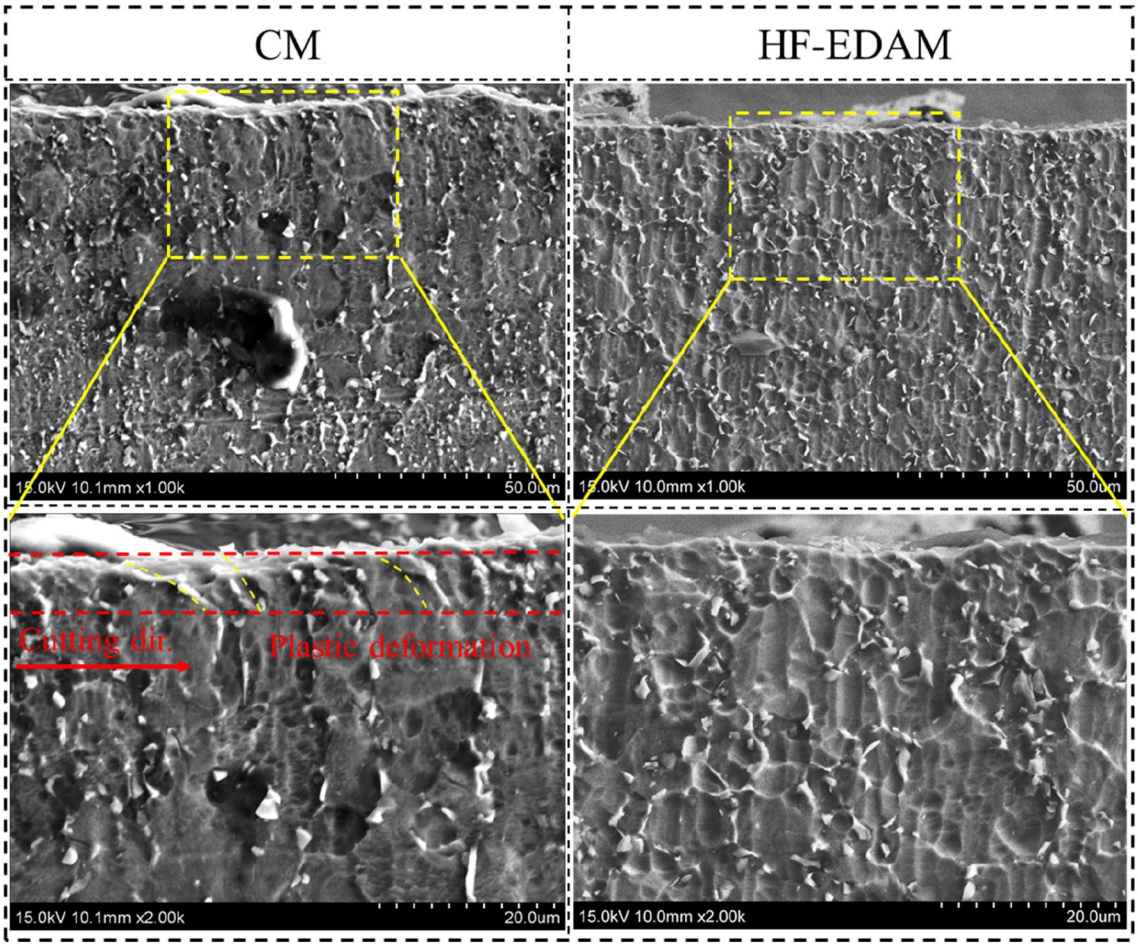

Fig. 26 Machined-Ti6Al4V subsurface plastic deformation in CM and HF-EDAM (with a capacitance of 100,000 pF) of Ti6Al4V, respectively, for a feed rate of 40 mm/min

Acknowledgements R.W. contributed equally to this work. This research was supported by the National Research Foundation of Korea (NRF) grant funded by the Korean Government (MSIT) (2020R1A2B5B02001755). Also, the authors gratefully acknowledge the financial support of the National Natural Science Foundation of China (No. 51905169) and the Natural Science Foundation of Hunan Province of China (2021jj40203).

Author Contributions MX: conceptualization, experiments, formal analysis, writing-original draft preparation, visualization, data curation. RW: validation, formal analysis, investigation, visualization. CL: conceptualization, supervision, resources. RK: measurement and data analysis. CJ: project administration. TJK: conceptualization, resources, visualization, supervision, project administration, funding acquisition.

Declarations

Conflict of Interest The authors declare that they have no known competing financial interests or personal relationships that could have appeared to influence the work reported in this paper.

References

1. Yang, X., & Richard Liu, C. (1999). Machining titanium and its alloys. *Machining Science and Technology, 3*(1), 107–139. https://doi.org/10.1080/10940349908945686
2. Narutaki, N., Murakoshi, A., Motonishi, S., & Takeyama, H. (1983). Study on machining of titanium alloys. *CIRP Annals, 32*(1), 65–69. https://doi.org/10.1016/s0007-8506(07)63362-9
3. Ezugwu, E. O., & Wang, Z. M. (1997). Titanium alloys and their machinability—A review. *Journal of Materials Processing Technology, 68*(3), 262–274. https://doi.org/10.1016/s0924-0136(96)00030-1
4. Liao, Z., la Monaca, A., Murray, J., Speidel, A., Ushmaev, D., Clare, A., & M'Saoubi, R. (2021). Surface integrity in metal machining—Part I: Fundamentals of surface characteristics and formation mechanisms. *International Journal of Machine Tools and Manufacture, 162*, 103687. https://doi.org/10.1016/j.ijmachtools.2020.103687
5. Dandekar, C. R., Shin, Y. C., & Barnes, J. (2010). Machinability improvement of titanium alloy (Ti-6Al-4V) via LAM and hybrid machining. *International Journal of Machine Tools and Manufacture, 50*(2), 174–182. https://doi.org/10.1016/j.ijmachtools.2009.10.013

6. Niu, Y., Jiao, F., Zhao, B., & Wang, D. (2017). Multiobjective optimization of processing parameters in longitudinal-torsion ultrasonic assisted milling of Ti-6Al-4V. *The International Journal of Advanced Manufacturing Technology, 93*(9–12), 4345–4356. https://doi.org/10.1007/s00170-017-0871-3
7. Yadav, U. S., & Yadava, V. (2015). Experimental modelling and optimisation of process parameters of hole drilling by electrical discharge machining of aerospace titanium alloy. *International Journal of Manufacturing Technology and Management, 29*(3/4), 211–234. https://doi.org/10.1504/ijmtm.2015.069256
8. Ayed, Y., Germain, G., Ben Salem, W., & Hamdi, H. (2014). Experimental and numerical study of laser-assisted machining of Ti6Al4V titanium alloy. *Finite Elements in Analysis and Design, 92*, 72–79. https://doi.org/10.1016/j.finel.2014.08.006
9. Al-Ahmari, A. M. A., Rasheed, M. S., Mohammed, M. K., & Saleh, T. (2015). A hybrid machining process combining micro-EDM and laser beam machining of nickel–titanium-based shape memory alloy. *Materials and Manufacturing Processes, 31*(4), 447–455. https://doi.org/10.1080/10426914.2015.1019102
10. Gu, L., Li, L., Zhao, W., & Rajurkar, K. P. (2012). Electrical discharge machining of Ti6Al4V with a bundled electrode. *International Journal of Machine Tools and Manufacture, 53*(1), 100–106. https://doi.org/10.1016/j.ijmachtools.2011.10.002
11. Goiogana, M., Sarasua, J. A., Ramos, J. M., Echavarri, L., & Cascón, I. (2016). Pulsed ultrasonic assisted electrical discharge machining for finishing operations. *International Journal of Machine Tools and Manufacture, 109*, 87–93. https://doi.org/10.1016/j.ijmachtools.2016.07.005
12. Lauwers, B., Klocke, F., Klink, A., Tekkaya, A. E., Neugebauer, R., & Mcintosh, D. (2014). Hybrid processes in manufacturing. *CIRP Annals, 63*(2), 561–583. https://doi.org/10.1016/j.cirp.2014.05.003
13. Kurniawan, R., Thirumalai Kumaran, S., Arumuga Prabu, V., Zhen, Y., Park, K. M., Kwak, Y. I., & Ko, T. J. (2017). Measurement of burr removal rate and analysis of machining parameters in ultrasonic assisted dry EDM (USHF-EDAM) for deburring drilled holes in CFRP composite. *Measurement, 110*, 98–115. https://doi.org/10.1016/j.measurement.2017.06.008
14. Li, C. P., Kim, M.-Y., Islam, M. M., & Ko, T. J. (2016). Mechanism analysis of hybrid machining process comprising EDM and end milling. *Journal of Materials Processing Technology, 237*, 309–319. https://doi.org/10.1016/j.jmatprotec.2016.06.022
15. Li, C., Xu, M., Yu, Z., Huang, L., Li, S., Li, P., Niu, Q., & Ko, T. J. (2020). Electrical discharge-assisted milling for machining titanium alloy. *Journal of Materials Processing Technology, 285*, 116785. https://doi.org/10.1016/j.jmatprotec.2020.116785
16. Li, C., Huang, L., Xu, M., Chen, Y., Chen, J., & Ko, T. J. (2022). Processing mechanism of electrical discharge-assisted milling titanium alloy based on 3D thermal-mechanical coupling cutting model. *Journal of Manufacturing Processes, 78*, 107–119. https://doi.org/10.1016/j.jmapro.2022.04.012
17. Xu, M., Li, C., Kurniawan, R., Park, G., Chen, J., & Ko, T. J. (2022). Study on surface integrity of titanium alloy machined by electrical discharge-assisted milling. *Journal of Materials Processing Technology, 299*, 117334. https://doi.org/10.1016/j.jmatprotec.2021.117334
18. Jung, S. T., Kurniawan, R., Thirumalai Kumaran, S., Yoon, I. J., & Ko, T. J. (2020). Mechanism study of micro-electrical discharge drilling method during micro-dimpling. *Journal of Mechanical Science and Technology, 34*, 2549–2559. https://doi.org/10.1007/s12206-020-0530-8
19. Yun, E., Lee, K., & Lee, S. (2004). Improvement of high-temperature hardness of (TiC, TiB)/Ti-6Al-4V surface composites fabricated by high-energy electron-beam irradiation. *Surface Coatings and Technology, 184*(1), 74–83.
20. Kurniawan, R., et al. (2017). Measurement of burr removal rate and analysis of machining parameters in ultrasonic assisted dry EDM (US-EDM) for deburring drilled holes in CFRP composite. *Measurement, 110*, 98–115.
21. Jithin, S., Bhandarkar, U. V., & Joshi, S. S. (2017). Analytical simulation of random textures generated in electrical discharge texturing. *Journal of Manufacturing Science and Engineering, 139*(11), 111002. https://doi.org/10.1115/1.4037322
22. Patel, M. R., et al. (1989). Theoretical models of the electrical discharge machining process II The anode erosion model. *Journal of Applied Physics, 66*(9), 4104–4111.
23. Shatla, M., & Altan, T. (2000). Analytical modeling of drilling and ball end milling. *Journal of Materials Processing Technology, 98*(1), 125–133.
24. Budak, E., Altintas, Y., & Armarego, E. J. A. (1996). Prediction of milling force coefficients from orthogonal cutting data. *Journal of Manufacturing Science and Engineering, 118*(2), 216–224.
25. Dudzinski, D., & Molinari, A. (1997). A modelling of cutting for visco-plastic materials. *International Journal of Mechanical Sciences, 39*(4), 369–389.
26. Manjunathaiah, J., & Endres, W. J. (2000). A new model and analysis of orthogonal machining with an edge-radiused tool. *Journal of Manufacturing Science and Engineering—Transactions of the ASME, 122*(3), 384–390.
27. Merchant, M. E. (1945). Mechanics of the metal cutting process. II. Plasticity conditions in orthogonal cutting. *Journal of Applied Physics, 16*(6), 318–324.
28. Waldorf, D. J., DeVor, R. E., & Kapoor, S. G. (1998). A slip-line field for ploughing during orthogonal cutting. *ASME J. Manuf. Sci. Eng., 120*(4), 693–699.
29. Hang, Z., Hao, Z., Rong, Y., Wei, W., & Fangyu, P. (2021). Analytical modeling of cutting forces considering material softening effect in laser-assisted milling of AerMet100 steel. *International Journal of Advanced Manufacturing Technology, 113*, 247–260.
30. Tounsi, N., Vincenti, J., Otho, A., & Elbestawi, M. A. (2002). From the basic mechanics of orthogonal metal cutting toward the identification of the constitutive equation. *International Journal of Machine Tools and Manufacture, 42*(12), 1373–1383.
31. Arrazola, P.-J., Garay, A., Iriarte, L.-M., Armendia, M., Marya, S., & Le Maître, F. (2009). Machinability of titanium alloys (Ti6Al4V and Ti555.3). *Journal of Materials Processing Technology, 209*(5), 2223–2230. https://doi.org/10.1016/j.jmatprotec.2008.06.020
32. Sun, J., & Guo, Y. B. (2008). A new multi-view approach to characterize 3D chip morphology and properties in end milling titanium Ti-6Al-4V. *International Journal of Machine Tools and Manufacture, 48*(12–13), 1486–1494. https://doi.org/10.1016/j.ijmachtools.2008.04.002
33. Li, H., & Wang, J. (2015). An experimental study of abrasive waterjet machining of Ti-6Al-4V. *The International Journal of Advanced Manufacturing Technology, 81*(1–4), 361–369. https://doi.org/10.1007/s00170-015-7245-5

Moran Xu is currently a master and doctor candidate in Mechanical Engineering of Yeungnam University, Korea. He received B. Eng degree from Hunan University of Science and Technology, China. He is interested in composite processing of difficult to process materials, ultrasonic vibration spindle and low-temperature green manufacturing research.

Rong Wei is currently a master candidate in Mechanical Engineering of Hunan University of Science and Technology, China. She received B. Eng degree from Yantai University, China. And she is interested in the research of composite processing of difficult-to-machine materials.

Changping Li received his M.S. and Ph. D from the Yeungnam University, Korea. Dr. Li is currently a teacher at College of Mechanical and Electrical Engineering. And Dr. Li is interested in the research of high-speed cutting and composite processing of difficult-to-machine materials.

Rendi Kurniawan is currently assistant professor in Yeungnam University, South Korea. He received B. Eng degree from Universitas Indonesia, Indonesia. His M. S. Eng degree in mechanical engineering was acknowledged from Yeungnam University, South Korea. He received Ph. D degree in mechanical engineering from Yeungnam University. His research interests are surface texturing, tribology, friction reduction, micro-dimple fabrication, and elliptical vibration texturing.

Jielin Chen is currently a master and doctor candidate in Mechanical Engineering of Yeungnam University, Korea. He received B. Eng degree from Hunan University of Science and Technology, China. He is interested in digital twin and intelligent manufacturing research.

Tae Jo Ko is a professor of mechanical engineering at Yeungnam University, South Korea. He received bachelor and master degrees from Pusan National Univestiry, South Korea. He received Ph.D. in mechanical engineering from POSTECH, South Korea. His research interests include development of machine tools, micro-cutting process, non-traditional machining, surface texturing using grinding, bio-machining, hybrid EDM-milling process, textured surface on cutting tools and deburring process of CFRP composite.